# Tumor ENPP1 (CD203a)/Haptoglobin Axis Exploits Myeloid-Derived Suppressor Cells to Promote Post-Radiotherapy Local Recurrence in Breast Cancer

Borja Ruiz-Fernández de Córdoba[1], Haritz Moreno[1], Karmele Valencia[1,2,3], Naiara Perurena[1], Pablo Ruedas[1], Thomas Walle[1], Alberto Pezonaga-Torres[1], Juan Hinojosa[1], Elisabet Guruceaga[4], Antonio Pineda-Lucena[5], Marta Abengózar-Muela[6], Denis Cochonneau[7,8], Carolina Zandueta[1], Susana Martínez-Canarias[1], Álvaro Teijeira[9], Daniel Ajona[1,2,3,10], Sergio Ortiz-Espinosa[1,2], Xabier Morales[11], Carlos Ortiz de Solórzano[11], Marta Santisteban[12], Luis I. Ramos-García[13], Laura Guembe[14], Vratislav Strnad[15], Dominique Heymann[7,8,16], Sandra Hervás-Stubbs[9], Rubén Pío[1,2,3,10], María E. Rodríguez-Ruiz[9,13], Carlos E. de Andrea[6], Silvestre Vicent[1,3,10,17], Ignacio Melero[3,10,12,17], Fernando Lecanda[1,3,10,17], and Rafael Martínez-Monge[3,12,13]

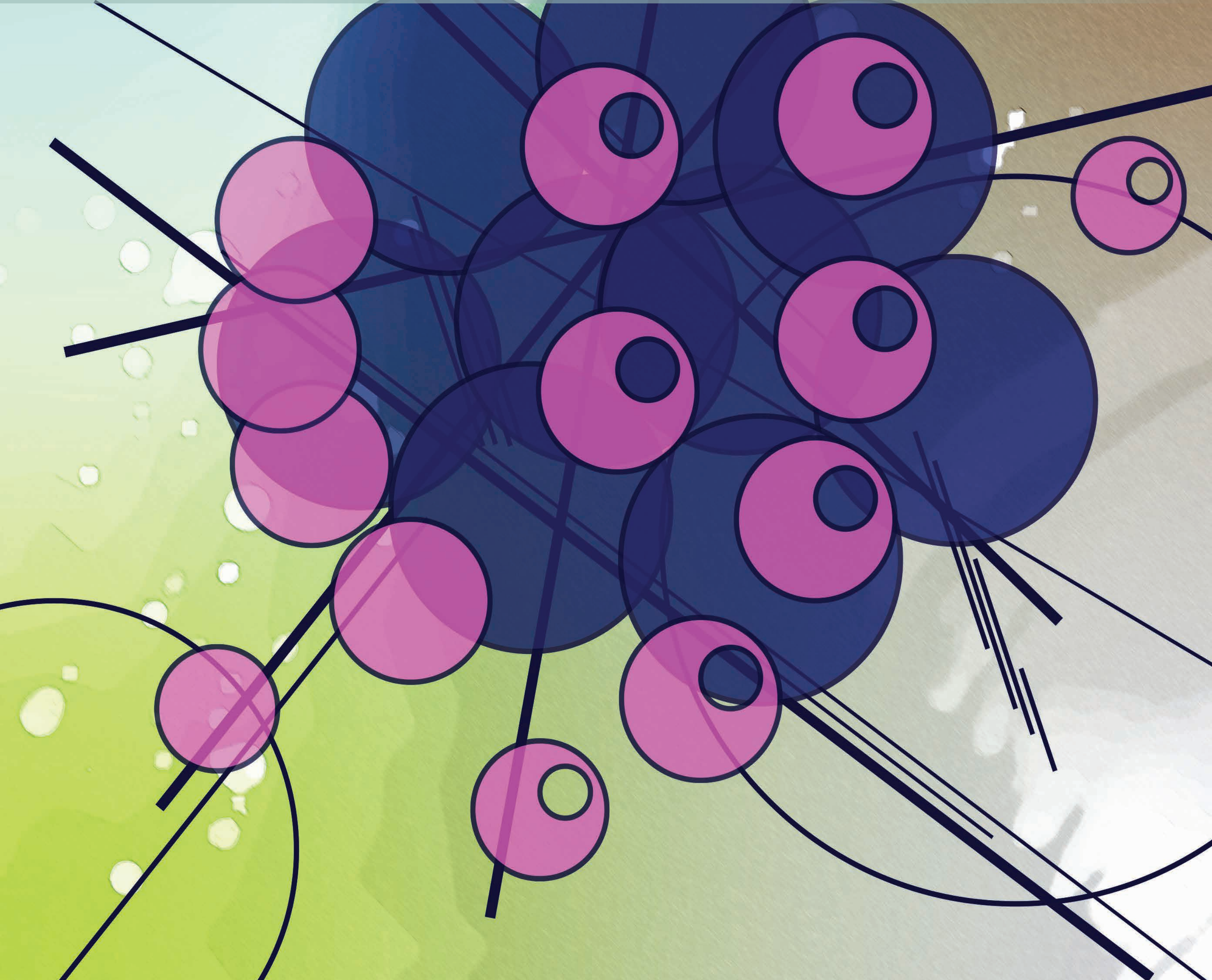

**ABSTRACT** Locoregional failure (LRF) in patients with breast cancer post-surgery and post-irradiation is linked to a dismal prognosis. In a refined new model, we identified ectonucleotide pyrophosphatase/phosphodiesterase 1/CD203a (ENPP1) to be closely associated with LRF. ENPP1$^{hi}$ circulating tumor cells (CTC) contribute to relapse by a self-seeding mechanism. This process requires the infiltration of polymorphonuclear myeloid-derived suppressor cells and neutrophil extracellular trap (NET) formation. Genetic and pharmacologic ENPP1 inhibition or NET blockade extends relapse-free survival. Furthermore, in combination with fractionated irradiation, ENPP1 abrogation obliterates LRF. Mechanistically, ENPP1-generated adenosinergic metabolites enhance haptoglobin (HP) expression. This inflammatory mediator elicits myeloid invasiveness and promotes NET formation. Accordingly, a significant increase in ENPP1 and NET formation is detected in relapsed human breast cancer tumors. Moreover, high ENPP1 or HP levels are associated with poor prognosis. These findings unveil the ENPP1/HP axis as an unanticipated mechanism exploited by tumor cells linking inflammation to immune remodeling favoring local relapse.

**SIGNIFICANCE:** CTC exploit the ENPP1/HP axis to promote local recurrence post-surgery and post-irradiation by subduing myeloid suppressor cells in breast tumors. Blocking this axis impairs tumor engraftment, impedes immunosuppression, and obliterates NET formation, unveiling new opportunities for therapeutic intervention to eradicate local relapse and ameliorate patient survival.

## INTRODUCTION

Breast cancer is the second most common cause of cancer mortality in women worldwide (1). Although 60% of cases are diagnosed as localized disease, 10% of treated women will still develop locoregional recurrence or failure (LRF) in spite of state-of-the-art therapy, reaching 25% in triple-negative and HER2 subtypes (2, 3). In contrast to current treatments for the primary tumor, which include surgery, radiation, and chemotherapy, LRF poses a therapeutic dilemma, as treatment options are scant and are associated with a dismal prognosis. Within each subtype, the two major determinants of post-surgical and post-irradiation LRF are large tumor size and inappropriate resection margins (R1 and R2), among other minor clinical and pathologic factors (4). These clinical observations posit the emergence of quiescent tumor cells left outside the surgical tumor margins, which, if they overcome the constraints imposed by ionizing radiation (IR), could subsequently become reactivated by microenvironmental cues. These cells are found in specialized niches of the tumor microenvironment (TME) and may preserve phenotypic plasticity and resilience to genotoxic stress (5). Along these lines, the resected tumor bed (RTB) fluid obtained in patients treated only with surgery stimulates an aggressive phenotype in cultured tumor cells, whereas this effect is almost completely abrogated when irradiation is applied (6).

Breast tumors also release circulating tumor cells (CTC) from the primary tumor as an early event (7). CTC are detected in 10% to 30% of patients with nonmetastatic breast cancer during tumor evolution (8, 9). CTC status is becoming more commonly evaluated in clinical practice (10) because CTC also confer prognostic value. Treatment efficacy can also be assessed by monitoring CTC over time as a prognostic marker to estimate the risk of recurrence (11). Nevertheless,

---

[1] Solid Tumors Program. Division of Oncology, Center for Applied Medical Research, University of Navarra (CIMA), Pamplona, Spain. [2] Department of Biochemistry and Genetics, School of Sciences, University of Navarra, Pamplona, Spain. [3] Centro de Investigación Biomédica en Red de Cáncer (CIBERONC), Madrid, Spain. [4] Bioinformatics Core Facility, Center for Applied Medical Research, University of Navarra (CIMA), Pamplona, Spain. [5] Program of Molecular Therapies, Center for Applied Medical Research, University of Navarra (CIMA), Pamplona, Spain. [6] Departament of Pathology, Clínica University of Navarra, Pamplona, Spain. [7] Nantes Université, CNRS, US2B, UMR 6286, Nantes, France. [8] Institut de Cancérologie de l'Ouest, Tumor Heterogeneity and Precision Medicine, Saint Herblain, France. [9] Immunology and Immunotherapy, CIMA, Pamplona, Spain. [10] IdiSNA, Navarra Institute for Health Research, Pamplona, Spain. [11] Image Core Facility, CIMA, Pamplona, Spain. [12] Oncology, Clínica University of Navarra, Pamplona, Spain. [13] Radiation Oncology, Clínica University of Navarra, Pamplona, Spain. [14] Morphology Core Facility, CIMA, Pamplona, Spain. [15] Department of Radiation Oncology, University of Erlangen, Erlangen, Germany. [16] Department of Oncology and Metabolism, Medical School, Sheffield, UK. [17] School of Medicine, Department of Pathology, Anatomy and Physiology, University of Navarra, Pamplona, Spain.

**Note:** Supplementary data for this article are available at Cancer Discovery Online (http://cancerdiscovery.aacrjournals.org/).

B. Ruiz-Fernández de Córdoba and H. Moreno contributed equally to this article.

F. Lecanda and R. Martínez-Monge share senior authorship of this article.

**Corresponding Authors:** Fernando Lecanda, Solid Tumors, Oncology Program, Center for Applied Medical Research (CIMA), University of Navarra, Pamplona 31008, Navarra, Spain. Phone: 34-948-194-700, ext. 812028; E-mail: flecanda@unav.es; and Rafael Martínez-Monge, Department of Radiation Oncology, Clínica Universidad de Navarra, University of Navarra, Avda. Pío XII s/n, Pamplona, Spain. Phone: 34-948-255-400, ext. 825844; E-mail: rmartinezm@unav.es

Cancer Discov 2022;12:1356–77

**doi:** 10.1158/2159-8290.CD-21-0932

only a fraction of CTC are capable of surviving with potential to generate productive local or distant metastases (12). In animal models, CTC reinfiltrate an established tumor or spread to target organs, initiating secondary outgrowths (13). Based on this, a CTC-mediated mechanism of "tumor self-seeding" may also cooperate in local tumor recurrence. Yet surgical manipulation and IR perturbs the RTB to the extent that this milieu may also impose constraints on CTC engraftment and colonization. This is in part due to the altered immune landscape associated with a local inflammatory reaction. Indeed, several leukocyte subpopulations might efficiently promote the antitumor immune attack on incipient engrafted CTC. In contrast, other tumor-infiltrating leukocytes could exert protumorigenic effects, including polymorphonuclear myeloid-derived suppressor cells (PMN-MDSC) and monocytic MDSC (MON-MDSC). PMN-MDSC constitute a heterogeneous subpopulation that share many morphologic and phenotypic characteristics of neutrophils (14). They emerge for their salient proangiogenic role and immunosuppressive effects in a variety of tumors (15). Yet, the immune–CTC cross-talk and cellular and molecular underpinnings involved in LRF remain largely unexplored despite their suspected relevance for breast cancer and for a large variety of solid tumors.

To systematically dissect these events, we developed a new breast cancer model of LRF post-surgery and post-IR, in which we identified ENPP1 (ectonucleotide pyrophosphatase phosphodiesterase 1, or CD203a), a member of the nonclassic adenosinergic CD38–ENPP1–CD73 pathway. ENPP1 catalyzes the hydrolysis of ATP to AMP and GTP to GMP, while generating inorganic pyrophosphates (16). ENPP1 also promotes the hydrolysis of cGAMP (17), a potent activator of the innate immune cyclic GMP–AMP synthase (cGAS)–stimulator of interferon genes (STING) pathway (18), which leads to strong immunosuppression and tumor progression (19). Extracellular release of ATP and AMP and their ENPP1-mediated hydrolysis products (20, 21) act as substrates to fuel adenosine (ADO) production by the classic adenosinergic CD39–CD73 pathway (22). These metabolites, specifically AMP and ADO, are known to tightly regulate immune responses acting on the purinergic (G-coupled) P1 receptors of immune cells (23, 24).

In this study, ENPP1$^{hi}$-expressing CTC were more fit to efficiently home and colonize the RTB during tumor recurrence. Engrafted tumor cells mediated an immunosuppressive TME characterized by the chemotactic infiltration of PMN-MDSC. Unexpectedly, tumor ENPP1 levels were comodulated with the proinflammatory protein haptoglobin (HP), an event mechanistically mediated by the autocrine signaling of extracellular ENPP1 hydrolysis products. HP was identified as a chemoattractant of MDSC and a novel unanticipated inducer of neutrophil extracellular trap (NET) formation. NET are extruded DNA meshes associated with cytotoxic enzymes released to the extracellular milieu that, aside from their antibacterial role, have been found to foster tumor progression and metastasis in mouse models (25). Conversely, genetic and pharmacologic ENPP1 inhibition or P1 receptor blockade abrogates PMN-MDSC recruitment. Moreover, inhibition of NET formation markedly extends relapse-free survival. More interestingly, a combination of ENPP1 pharmacologic blockade and standard radiotherapy treatment post-surgery eradicates LRF.

Furthermore, patients with ENPP1$^{hi}$ or HP$^{hi}$ triple-negative breast cancer (TNBC) were associated with a worse prognosis and with tumor recurrence. Recurrent tumors showed an increased NET formation as compared with primary paired tumors. Thus, the ENPP1/HP axis illuminates a novel mechanism involved in breast LRF.

## RESULTS

### Establishment of a Breast Cancer Model of LRF

To set up a valuable model of LRF, we selected two triple-negative aggressive syngeneic breast cancer cell lines, ANV5 and 4T1, to develop murine orthotopic tumors in syngeneic mice. In pilot experiments, we injected these luciferase-transduced tumor cells in a small group of immunosuppressed mice, to evaluate the quality of the surgical procedure by bioluminescence imaging (BLI). The experimental scheme is represented in Fig. 1A. We used a brachytherapy technique by implanting a catheter into the RTB at the time of surgery for inserting the IR source (Supplementary Fig. S1A–S1C). Briefly, ANV5 tumor cells were inoculated in the inguinal mammary gland of syngeneic mice. Tumors were resected at ~300 ± 164 mm$^3$ tumor volume. Mice were randomized to receive 15 Gy IR or no further treatment. In this group, the procedure for the placement of catheters was performed with no IR. No differences in tumor volume between groups were detected at surgery (Fig. 1B). Excised tumors were ink-embedded for surgical border-free assessment (Fig. 1B). The characteristics of treated mice are shown in Supplementary Table S1. No differences in the quality of surgical resection were detected by histologic evaluation (Supplementary Table S2). Interestingly, local control in the resected group only (Sg) was 44.8%, whereas in the resected and IR group it was 62.2% (Fig. 1C).

The extent of the surgical margin was a critical factor associated with LRF (Fig. 1D). Although no differences were detected in tumor size at surgery, the R1 subgroup obtained the greatest advantage from the use of radiation (Fig. 1E), a finding consistent with the clinical observations (Supplementary Fig. S2). Surgical margins and treatment arm were the main predictors of local control in a multivariate analysis (Supplementary Table S3). Hence, IR decreased the rate of local relapse and prolonged the time to LRF. Gross necropsy analysis did not detect development of macroscopic distant metastasis in this model.

In a similar approach using the murine breast cancer 4T1 cells, we found a trend toward a longer relapse-free survival rate in the locally irradiated group as compared with untreated animals that did not reach statistical significance, but we observed spontaneous animal death associated with aggressive lung metastasis preventing the evaluation of LRF.

### Detection of CTC during Tumor Progression and Resection

Using microfluidics CTC detection technology (Parsortix), we evaluated the number of CTC pre- and post-surgery in the 4T1 and ANV5 models (Supplementary Fig. S3A). After bilateral orthotopic injection of 4T1 cells transduced with a GFP

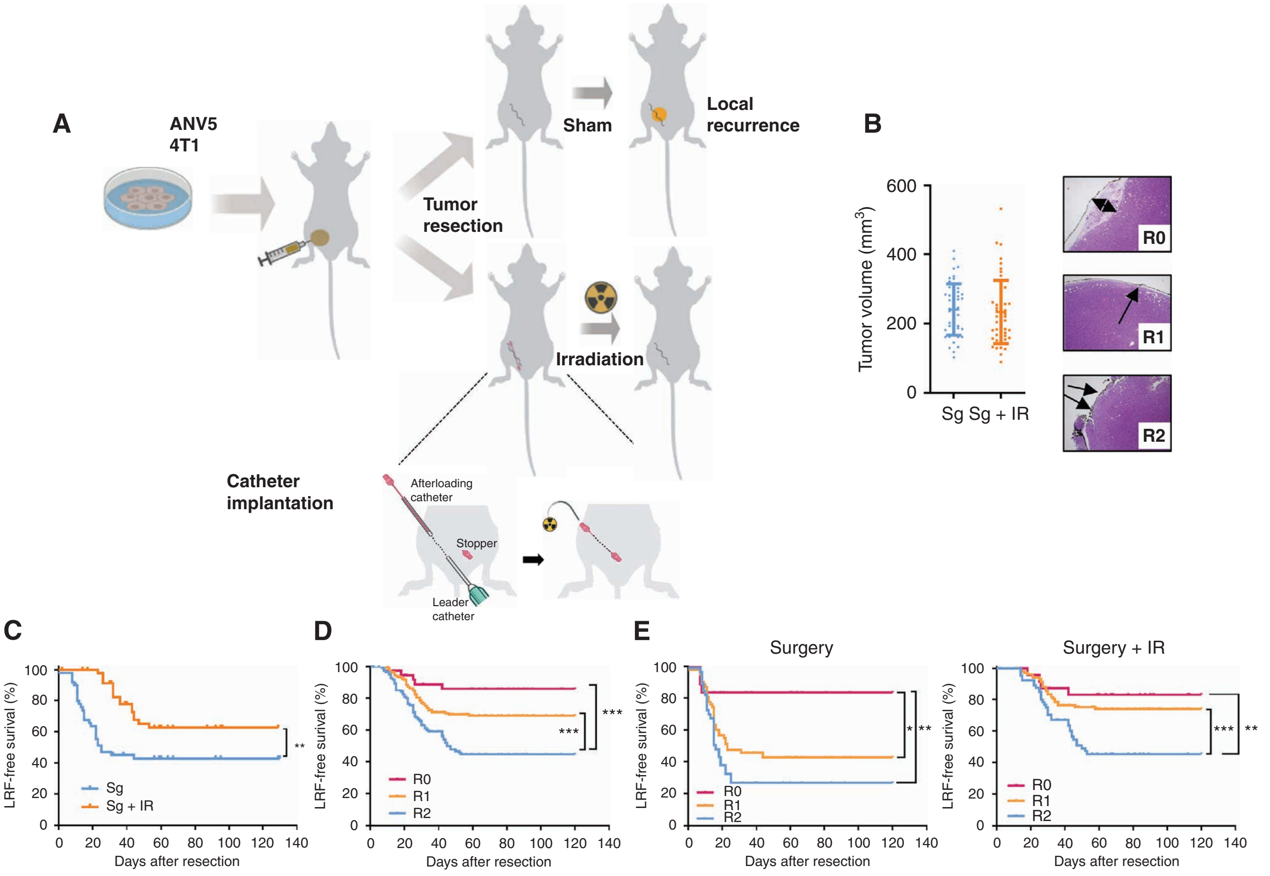

**Figure 1.** Model of LRF and its evaluation after surgical resection alone and post-radiation. **A,** Scheme of the LRF model. Murine syngeneic ANV5 or 4T1 tumor cells were injected in the fourth pair inguinal mammary gland by a surgical procedure. After tumor resection, animals were randomized to receive 15 Gy of irradiation through a catheter either implanted during resection or sham implanted. Bottom, scheme of the implantation of the afterloader catheter (red) through a leader catheter (gray) over the mammary gland. Once the afterloader catheter was introduced, the leader was pulled out, and a plastic bottom (stopper) was placed on the leader tip to allow its immobilization. **B,** Resection was performed when tumors reached the indicated size (Sg, only surgery; Sg + IR, surgery and irradiation). Tumor volume at resection is shown. Histologic assessment was performed after ink-staining of surgical margins. R0 denotes clear margins (double-headed arrow indicates normal breast tissue between the tumor edge and the inked margin), R1 denotes microscopically positive margin (arrow points at inked tumor edge), and R2 denotes incomplete gross resection (arrows point at area with tumor fragmentation). **C,** LRF-free survival after tumor resection assessed by tumor palpation and validation by histologic analysis for both treatments ($n = 50$ mice/group). No differences in tumor margins were detected. **D,** LRF-free survival showing groups segregated by tumor-resection margins (R0, R1, and R2 included $n = 43$, 174, and 108 mice, respectively). **E,** LRF-free survival in both treatments showing that irradiation (15 Gy) improves local control (left; R0, R1, and R2 contained $n = 18$, 64, and 41 mice, respectively) and that local control is margin dependent (right; R0, R1, and R2 contained $n = 25$, 110, and 67 mice, respectively). LRF relapse-free survival shows that the irradiation was more advantageous in R1 cases. Log-rank test was used. (*continued on next page*)

reporter gene, tumors were resected. Interestingly, the number of CTC in blood was markedly increased four hours after surgery compared with one day before surgery (Supplementary Fig. S3B and S3C). In the ANV5 model, an increase in the CTC number was detected post-surgery, although the number of CTC was very low in comparison with the 4T1 model (Supplementary Fig. S3B and S3C). Thus, CTC are commonly detected during primary tumor growth in both models. A few hours after tumor resection, the CTC number increases, suggesting a possible tumor-release effect during the surgical procedure.

## CTC Contribute to Local Recurrence

To investigate the causal link between CTC and LRF, we orthotopically inoculated naïve ANV5 cells in the mammary gland (day 0). At the time of tumor resection (day 17), the contralateral mammary gland was partially excised as a sham-surgery control. Subsequently, luciferase-GFP–transduced ANV5 cells were intracardiacally (i.c.) inoculated to mimic CTC (Fig. 1F). BLI assessed *in vivo* during follow-up revealed an increased signal in the RTB (ipsilateral mammary gland) that increased over time as compared with the contralateral mammary gland (Fig. 1G), although there was also an initial BLI detected in the contralateral mammary gland that disappeared over time. Interestingly, BLI was obliterated in IR mice. More importantly, immunohistochemical (IHC) analysis of recurrent tumors revealed the presence of several patches of GFP$^+$ cells within the tumor mass. This approach enabled us to detect CTC derived from i.c. inoculation that engrafted in the RTB and contributed to the formation of recurrent tumors. These findings were further substantiated

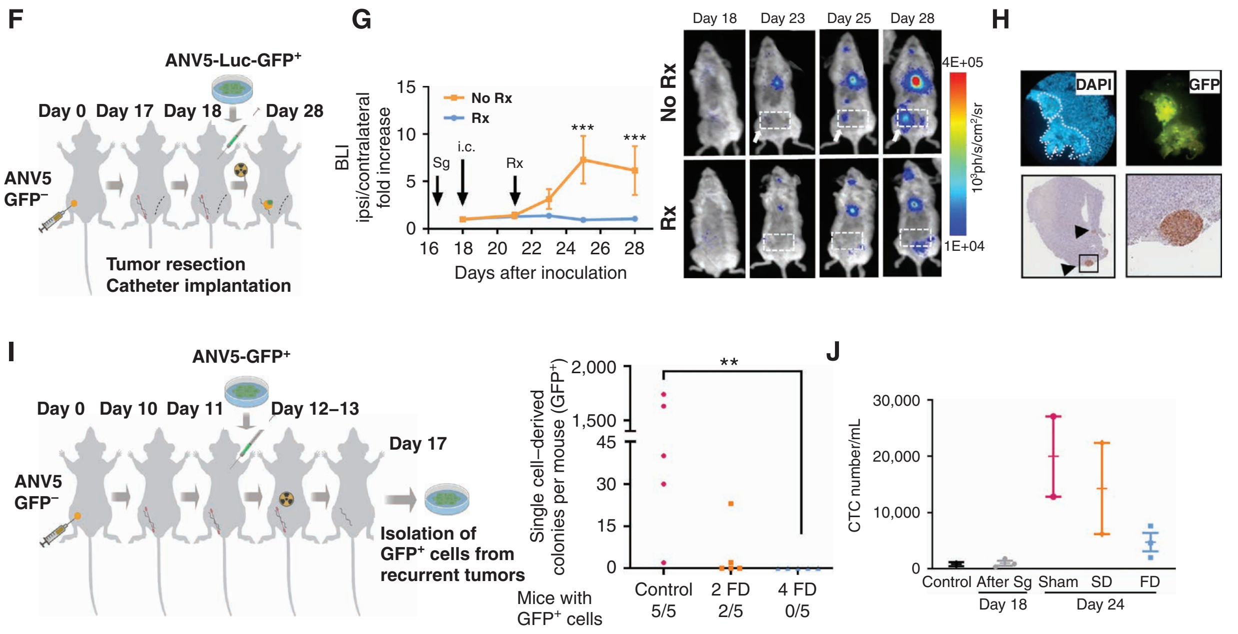

**Figure 1.** *(Continued)* **F,** Mice were injected in the right inguinal mammary gland with ANV5 cells according to the outline ($n = 10$ per group). Tumors were resected (day 17), and a partial mastectomy of the contralateral mammary gland served as a surgical control. One day after tumor resection, Luc-GFP+ cells mimicking CTC were inoculated in the left cardiac ventricle. Four days after resection (day 21) one group received 15 Gy radiation (IR), whereas the other group was non-IR. Local relapses (orange circle) were resected to assess the colonization of CTC (green dot). **G,** BLI was evaluated *in vivo* over time in the ipsilateral (white arrow) and contralateral mammary glands. The BLI signal in the RTB was detected and sustained only in non-IR (No Rx) mice and was obliterated in IR (Rx) mice. Mean ± SEM are represented. Two-way ANOVA was used for comparison. Representative images of BLI are shown for each time point, indicating a high signal in the RTB in non-IR mice (top). Arrow points to ipsilateral mammary gland. **H,** Top, fluorescence imaging of two consecutive sections of a tumor stained with DAPI and the detection of intense GFP+ cells of tumors arising in ANV5-Luc-GFP+–injected mice. Bottom, detection of GFP+ cells by IHC of tumors obtained 10 days after resection. Left, arrows indicate GFP+ colonies into the local relapses. Right, a detail of GFP+ cells from the left. **I,** Left, outline of the experimental setting. Mice ($n = 5$ per group) were injected with ANV5 cells. After resection (day 10), animals were i.c. inoculated with ANV5-GFP+ cells (day 11). The first group was sham-IR, the second group received 2 fractions (2 FD: 2 × 6.2 Gy) the same day and the third group received 4 fractions (4FD: 4 × 6.2 Gy) each delivered at least 6 hours apart in two consecutive days. On day 17, mice were sacrificed and mammary gland was minced to single-cell suspension and cultured in antibiotic medium. Only ANV5-GFP+ resistant cells were able to survive and form single cell–derived colonies. Right, quantification of resistant clones in each group is provided with representative images. Kruskal–Wallis test was used for comparison. **J,** Mice ($n = 3$ per group) were injected with 4T1 cells in the right inguinal mammary gland. After tumor resection (day 18), the first group was sham-IR, the second group received SD (15 Gy), and the third group received FD of 24.8 Gy in 4 fractions of 6.2 Gy each delivered at least 6 hours apart on two consecutive days. Blood was extracted 4 hours after surgery (Sg), and 6 days after surgery in all three groups (right). The number of CTC was assessed by Parsortix in exsanguinated mice showing a substantial decrease in FD group. Mean ± SEM are represented. *, $P < 0.05$; **, $P < 0.01$; ***, $P < 0.001$.

by assessing the fluorescently labeled cells GFP+ within the tumor (Fig. 1H). Similar results were obtained in the 4T1 model (Supplementary Fig. S3D and S3E). We also noted a strong signal emanating from the thoracic cavity, a finding consistent with the mediastinal contamination after i.c. inoculation and with the emergence of pulmonary metastases, an event profusely described in this model. These data thus suggest the proclivity of CTC to engraft in the RTB and contribute to the formation of the recurrent tumor mass.

## Radiation Differentially Eradicates CTC, Impairing LRF

Next, we sought to compare the efficacy of two irradiation regimens using single dose (SD) of 15 Gy versus fractionated dose (FD) of four fractions of 6.2 Gy equi-effective IR doses in both models, ANV5 or 4T1 cells (Supplementary Fig. S3F and S3G).

To evaluate whether this IR effect was due to the efficient eradication of engrafted CTC, we assessed the number of CTC homing and engrafting to the RTB with different FD (Fig. 1I). Briefly, after tumor resection, i.c. inoculation of ANV5-GFP+ was performed to mimic CTC. One group was 2FD-IR (2 × 6.2 Gy) and the other was 4FD-IR (4 × 6.2 Gy). The control group was sham-IR. At sacrifice, single-cell suspensions derived from total minced mammary glands were cultured *ex vivo*. Interestingly, a high number of clones derived from GFP+ single cells were isolated from sham-IR animals. In contrast, few clones were detected in any of the 2FD group and none in the 4FD group, indicating efficient IR-mediated eradication of GFP+ CTC-engrafted cells (Fig. 1I). We hypothesized that CTC could still engraft several days post-IR. We evaluated the number of CTC post-resection after 2FD or 4FD treatment by microfluidics in mice injected with 4T1-GFP+ cells in two mammary glands per mouse. After surgery, one group of animals was irradiated with an SD two days after surgery, the second group was FD-IR, and control mice were sham-IR. Blood samples were collected four days after tumor IR and seven days post-surgery (Fig. 1J). A slight decrease in the number of CTC was observed after SD (Fig. 1J) and a substantial decrease in the number of CTC was observed in the FD group. However, a small number of CTC were still detected after FD, indicating that these CTC could still be competent to engraft and contribute to LRF. Furthermore, local IR eradicates CTC engrafting in the RTB, and the IR schedule also has an impact on the number of CTC. Overall, CTC represent a determining factor contributing to the emergence of tumor recurrence. Interestingly, CTC after FD or SD were competent to give rise to local recurrence in the ANV5 model (using a similar approach as in Fig. 1F), an event associated with a diminished number of CTC colonizing the RTB (Supplementary Fig. S3H–S3K).

## Identification of a Transcriptomic Program of LRF

As engraftment represents a highly inefficient process, we obtained a marked relapsed phenotype by successive cycles of enrichment. Briefly, we isolated cell subpopulations from recurrent non-IR and IR tumors in the ANV5 model (Fig. 2A). Relapse-free survival curves showed a shorter latency time of recurrence for the cell lines 720Cy2Rx and 701Cy2Rx derived from second cycles in IR conditions, indicating an enrichment in the LRF phenotype (Fig. 2B).

To identify the determinants of the acquisition of increased competencies for LRF, we performed a transcriptomic analysis using RNA sequencing (RNA-seq) comparing parental ANV5 cells with second cycle IR cell subpopulations (Fig. 2C). Clustering analysis represents a selection of differentially expressed genes, one of which encodes for ENPP1 (19). We also performed a transcriptomic analysis comparing ANV5 with the second cycle isolated cells from IR and non-IR recurrent tumors (Supplementary Fig. S4A and S4B), a signature that was further validated in non-IR and IR tumors (Fig. 2D). Cells showed higher protein expression levels over increased cycles in ANV5 as compared with parental cells (Fig. 2E). Similar results were validated in 4T1 cells following an identical strategy (Supplementary Fig. S4C and S4D). Thus, the acquisition of an LRF-enriched phenotype is mediated by a common gene transcriptomic program, which is conserved irrespective of radiation conditions.

## CTC Enrichment of an ENPP1$^{hi}$ Phenotype

Based on previous findings, we reasoned that CTC could be enriched in LRF gene signature. To test this hypothesis, we isolated CTC from the blood of incipient orthotopically implanted 4T1-derived tumors, which release high numbers of CTC. These cells, called “CTC-out,” were expanded *ex vivo* and GFP transduced (Fig. 2F). These CTC-out cells showed similar levels of ENPP1 to the control 4T1 cells (Fig. 2G). Subsequently, in resected mice carrying 4T1 unlabeled mammary tumors, previously isolated CTC-out were i.c. inoculated with GFP$^+$ CTC-out cells ($n = 10$ mice per each CTC-out subpopulation). After recurrence, tumors were digested and GFP$^+$ cells isolated (called “CTC-in”). To further enrich this phenotype, recovered cells were subjected to another cycle of i.c. inoculation. ENPP1 expression levels were found elevated in all isolated CTC-in subpopulations as compared with control and CTC-out cells (Fig. 2G and H). To extend these results to the ANV5 model, we had to perform several cycles after i.c. inoculation of GFP$^+$ ANV5 cells in mice previously tumor resected to obtain CTC-in cells, as we were unsuccessful at isolating CTC-out. Interestingly, ENPP1 gene-expression levels in CTC-in of different cycles consistently showed an enrichment in ENPP1 in recurrent tumors (Fig. 2G and H). Other components including SRPX2 and EPAS1 showed no consistent expression levels in CTC-in cells (Supplementary Fig. S5A and S5B). Interestingly, varied ENPP1 expression levels were found in cancer cell lines derived from different tumors (Supplementary Fig. S5C).

Next, we investigated whether ENPP1 levels could endow cells with an advantageous function for homing and engraftment at the RTB. We overexpressed ENPP1 (OE-ENPP1) in ANV5-GFP$^+$ cells. Cells were i.c. inoculated one day after resection of ANV5-derived tumor (Fig. 2I). Interestingly, mice inoculated with OE-ENPP1-GFP$^+$ cells showed an increased number of single cell–derived colonies obtained from the resected mammary glands at day 6 post-inoculation with no effect on cell growth kinetics *in vitro* (Fig. 2I). We also found that ENPP1$^{hi}$ cells were endowed with increased radioresistance (Supplementary Fig. S5D). Thus, ENPP$^{hi}$ CTC showed an enhanced ability to engraft in the RTB.

## Functional Contribution of ENPP1 to LRF

We assessed the functional contribution of ENPP1 in LRF using ENPP1 (OE-ENPP1) and parental ANV5 cells (control; Fig. 3A). After tumor resection, local recurrence was evaluated by histology. Tumor volume was matched between groups before surgery. A diminished recurrence-free survival of OE-ENPP1–derived tumors was detected over control mice (Fig. 3B and C).

We also silenced *Enpp1* (sh*Enpp1*) in 720Cy2Rx cells (Fig. 3D). Tumor volume was matched between groups before surgery. Interestingly, Kaplan–Meier curves of relapse-free survival showed an extended time to LRF in sh*Enpp1*-derived tumors with a survival rate around 70% (Fig. 3E). In the LRF model, similar tumor volumes were reached in both groups before surgery (Fig. 3F).

As ENPP1 has been categorized as an immunotransmitter, we evaluated whether ENPP1 levels could modulate tumor-associated immune infiltrate. First, we estimated the relative levels of the ENPP1 diesterase activity in parental ANV5, 720Cy2Rx, and these cells transduced with two different shRNAs targeting *Enpp1* (Supplementary Fig. S5E), and we assessed the immune landscape after orthotopic injection (Supplementary Fig. S6A and S6B).

At day of sacrifice, tumors derived from sh*Enpp1* cells showed a significant decrease in tumor volume (Fig. 3G). Moreover, tumors derived from *Enpp1*-silenced cells showed a consistent decrease in total myeloid cells and PMN-MDSC (CD11b$^+$Ly6C$^{lo}$Ly6G$^+$) and CD4$^+$ regulatory T cells (Treg), whereas CD8$^+$ T cells, including effector subsets, were unaffected (Supplementary Fig. S7A and S7B).

A converse experiment was performed using forced expression of ENPP1 (OE-ENPP1) in ANV5 cells. A significant increase in orthotopic tumor volume was observed (Fig. 3H). Interestingly, a significant increase in total myeloid cells CD11$^+$ with an increase in PMN-MDSC ($P < 0.01$) was detected in OE-ENPP1–derived tumors, whereas no changes were detected in Tregs (Fig. 3H). CD8$^+$ and CD4$^+$ effector

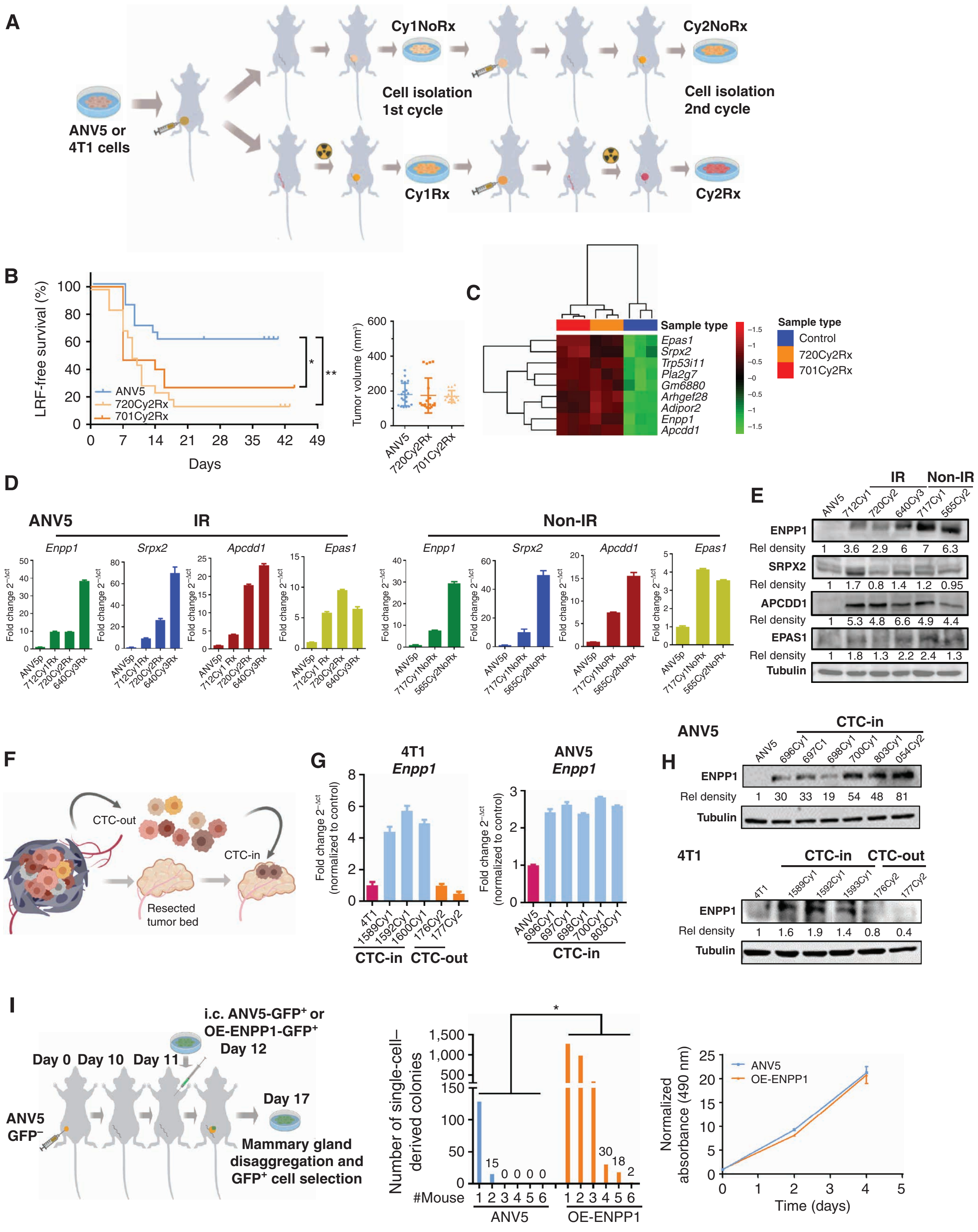
A
ANV5 or
4T1 cells
Cy1NoRx
Cell isolation
1st cycle
Cy2NoRx
Cell isolation
2nd cycle
Cy1Rx
Cy2Rx
B
LRF-free survival (%)
100
80
60
40
20
0
0 7 14 21 28 35 42 49
Days
ANV5
720Cy2Rx
701Cy2Rx
*
**
Tumor volume (mm³)
600
400
200
0
ANV5
720Cy2Rx
701Cy2Rx
C
Sample type
Epas1
Srpx2
Trp53i11
Pla2g7
Gm6880
Arhgef28
Adipor2
Enpp1
Apcdd1
1.5
1
0.5
0
−0.5
−1
−1.5
Sample type
Control
720Cy2Rx
701Cy2Rx
D
ANV5
IR
Non-IR
Enpp1
Srpx2
Apcdd1
Epas1
Fold change 2^−Δct
ANV5p
712Cy1Rx
720Cy2Rx
640Cy3Rx
717Cy1NoRx
565Cy2NoRx
E
IR
Non-IR
ANV5
712Cy1
720Cy2
640Cy3
717Cy1
565Cy2
ENPP1
Rel density 1 3.6 2.9 6 7 6.3
SRPX2
Rel density 1 1.7 0.8 1.4 1.2 0.95
APCDD1
Rel density 1 5.3 4.8 6.6 4.9 4.4
EPAS1
Rel density 1 1.8 1.3 2.2 2.4 1.3
Tubulin
F
CTC-out
CTC-in
Resected
tumor bed
G
4T1
Enpp1
Fold change 2^−Δct
(normalized to control)
8
6
4
2
0
4T1
1589Cy1
1592Cy1
1600Cy1
176Cy2
177Cy2
CTC-in
CTC-out
ANV5
Enpp1
3
2
1
0
ANV5
696Cy1
697Cy1
698Cy1
700Cy1
803Cy1
CTC-in
H
ANV5
CTC-in
ANV5
696Cy1
697C1
698Cy1
700Cy1
803Cy1
054Cy2
ENPP1
Rel density 1 30 33 19 54 48 81
Tubulin
4T1
CTC-in
CTC-out
4T1
1589Cy1
1592Cy1
1593Cy1
176Cy2
177Cy2
ENPP1
Rel density 1 1.6 1.9 1.4 0.8 0.4
Tubulin
I
Day 0
Day 10
Day 11
i.c. ANV5-GFP⁺ or
OE-ENPP1-GFP⁺
Day 12
Day 17
ANV5
GFP⁻
Mammary gland
disaggregation and
GFP⁺ cell selection
Number of single-cell–
derived colonies
1,500
1,000
500
150
100
50
0
*
15
0 0 0 0
30
18
2
#Mouse 1 2 3 4 5 6 1 2 3 4 5 6
ANV5
OE-ENPP1
Normalized
absorbance (490 nm)
25
20
15
10
5
0
0 1 2 3 4 5
Time (days)
ANV5
OE-ENPP1

cells were unaffected. By contrast, we found a diminished number of natural killer (NK) and dendritic cells infiltrating OE-ENPP1 tumors (Supplementary Fig. S7C). The infiltration kinetics of PMN-MDSC in the RTB were measured at early time points (days 1, 6, and 8) post-injection in mice ($n = 8$ per time point) injected with OE-ENPP1 cells (Fig. 3I). Interestingly, at days 6 and 8 post-injection when the tumors were barely palpable, increasing numbers of infiltrated PMN-MDSC were already detected. Conversely, ENPP1-silenced tumors showed a significantly decreased number of infiltrated PMN-MDSC at day 13 (Fig. 3J).

Thus, a steady infiltration kinetics of PMN-MDSC concurrent with tumor cell colonization of the RTB was detected from early phases of tumor growth. Moreover, modulation of ENPP1-tumor levels regulated the immune landscape by consistently altering PMN-MDSC tumor infiltration.

## PMN-MDSC Contribute to LRF

To discriminate the functional role of PMN-MDSC infiltration, we depleted PMN-MDSC with an anti-Gr1$^+$ antibody in an orthotopic model of tumor growth using OE-ENPP1 and control ANV5 cells. At day 15, we observed an expected increase in tumor volume in OE-ENPP1–derived tumors until sacrifice. Interestingly, anti-Gr1–treated animals inoculated with OE-ENPP1 cells showed a dramatic decrease in tumor volume, reaching a similar size to tumors derived from control mice ($P < 0.0001$; Fig. 3K). No changes in tumor volume were detected in control animals treated with anti-Gr1 antibody. Blood counts of neutrophils were significantly diminished at sacrifice (two days after last depletion) in the Gr1$^+$-treated OE-ENPP1 group (Fig. 3L), whereas no significant changes were detected in the number of lymphocytes. IHC analysis showed a decreased number of tumor-infiltrating Gr1$^+$ cells in OE-ENPP1 tumors treated with anti-Gr1 in correlation with tumor volumes (Fig. 3M).

Next, we performed an LRF assay with OE-ENPP1 and control cells. Tumors were resected at similar tumor volume (Fig. 3N). As expected, OE-ENPP1–injected animals showed an accelerated LRF rate. Interestingly, the LRF rate diminished in the anti-Gr1–treated group injected with OE-ENPP1 cells, whereas anti-Gr1 treatment had no effect in mice injected with control cells (Fig. 3N). IHC analysis revealed a decrease in the Gr1$^+$ infiltrate in Gr1-depleted tumors overexpressing ENPP1 as compared with vehicle-treated OE-ENPP1–derived tumors (Fig. 3O). These findings indicate that Gr1$^+$ cell subpopulations were associated with ENPP1 tumor expression levels. The Gr1$^+$ cell subpopulations played a significant immune-mediated role in orthotopic tumor growth and in LRF-free survival rate.

## Pharmacologic Inhibition of ENPP1 Blocks LRF

Next, we interrogated the efficacy of pharmacologic blockade of ENPP1 using a small-molecule ENPP1 inhibitor (ENPP1i; CM3163), whose activity was tested *in vitro* (Supplementary Fig. S7D; ref. 19). In an orthotopic experiment using a 4T1 subpopulation (374Cy2NoRx cells) that expresses high ENPP1 levels, tumor volume of treated mice decreased in comparison with vehicle-treated mice (Supplementary Fig. S7E). In orthotopic tumors inoculated with 720Cy2Rx cells, a significant decrease in PMN-MDSC in ENPP1i-treated animals was found in an independent experiment performed where ENPP1i also decreased tumor volume. We also detected an increase in NK, CD8$^+$ T effector, and dendritic cells and a decrease in tumor-associated macrophages and M2 macrophages in ENPP1-treated mice (Fig. 4A). Thus, ENPP1 inhibition strongly remodels the tumor-associated immune landscape, mounting a marked antitumor effector response.

In an LRF assay using the ENPP$^{hi}$ ANV5 subpopulation (720Cy2Rx), ENPP1i diminished the LRF rate and extended relapse-free survival (Fig. 4B). Abrogation of other cell subpopulations including CD8$^+$ T or NK cells in this assay did not significantly influence relapse-free survival. IHC analysis showed a decreased number of Gr1$^+$ leukocytes infiltrating the tumors in ENPP1i-treated mice (Fig. 4B). Interestingly, the STING pathway was also partially mediating ENPP1 function on tumor growth *in vivo*, as codepletion of STING (C-176) in control or silenced ENPP1 cells led to increased tumor growth kinetics (Fig. 4C). Furthermore, codepletion of CD39 in ENPP1-silenced tumor cells led to a significant increase in LRF-free survival rate (Fig. 4D), an effect presumably mediated by the immune compartment as ANV5 cells were devoid of CD39.

To evaluate whether ENPP1i therapy could benefit the current standard of care (surgery and fractionated IR), ENPP1i

**Figure 2.** CTC are enriched in ENPP1. **A,** Outline of the strategy used to enrich the LRF phenotype with and without IR (15 Gy) by isolation and expansion of recurrent cells and reinoculation in another cohort of mice. Cy1NoRx: cycle 1 with no radiation. Cy1Rx: cycle 1 with radiation. **B,** Left, relapse-free survival rate between ANV5 control and two different second cycle irradiated cell subpopulations (720Cy2Rx and 701Cy2Rx). Log-rank test was used. Right, tumor volume at resection. No differences in tumor margins between groups were detected ($n = 20$ mice in ANV5 and 720Cy2Rx and $n = 15$ mice in 701Cy2Rx). **C,** Hierarchical cluster diagram of top differentially expressed genes in control ANV5 cells and two second cycle IR cell subpopulations. **D,** Gene-expression levels of the indicated genes evaluated by RT-qPCR in cell lines derived from different *in vivo* cycles (Cy1, Cy2, and Cy3) in IR (Rx) and non-IR conditions (no Rx). **E,** Western blot analysis of ENPP1 levels in cells isolated in different cycles. Quantification of relative expression levels is shown. **F,** Scheme showing the CTC isolation in the blood, called "CTC-out," derived from the primary tumor, whereas CTC reaching the RTB were called "CTC-in." CTC-out cells isolated from blood were orthotopically implanted in another cohort of mice and reisolated to obtain CTC-out cells of cycle 2 (Cy2). To obtain CTC-in, second cycle labeled CTC-out were i.c. inoculated (50,000 cells) after tumor resection composed of unlabeled tumor cells. Different CTC-in cells were isolated for 4T1 cells. For ANV5, CTC-out were technically impossible to isolate in this model, and so we i.c. inoculated labeled ANV5-GFP$^+$ cells (100,000 cells) into tumor-resected mice (originated from unlabeled ANV5 cells) to obtain CTC-in. **G,** In the 4T1 model, gene-expression levels of *Enpp1* were evaluated by RT-qPCR in a panel of CTC isolated in several rounds of CTC-out and in CTC-in. In the ANV5 model, *Enpp1* expression levels were evaluated in a panel of CTC-in. **H,** Western blot analysis of ENPP1 levels in CTC-in cells isolated in different cycles for ANV5 and CTC-in, and CTC-out for 4T1 cells. **I,** Left, scheme for the isolation of GFP$^+$ cells either ANV5 (mock-transduced) or ENPP1-overexpressing cells (OE-ENPP1), i.c. inoculated one day post-resection of the GFP$^-$ tumor. The sixth day after i.c inoculation, mammary gland was disaggregated, minced to single-cell suspension, and cells were incubated in the presence of selection antibiotic puromycin for 2 weeks. Middle, quantification of all resistant single cell–derived colonies for each mouse. Mann–Whitney test was used for comparison. Bottom, representative image of single cell–derived colonies stained with crystal violet. Right, cell growth kinetics *in vitro* using MTS assay. Data were normalized with absorbance at day 0 and represent mean ± SD of six replicates. Experiment was performed three times with similar results. *, $P < 0.05$; **, $P < 0.01$.

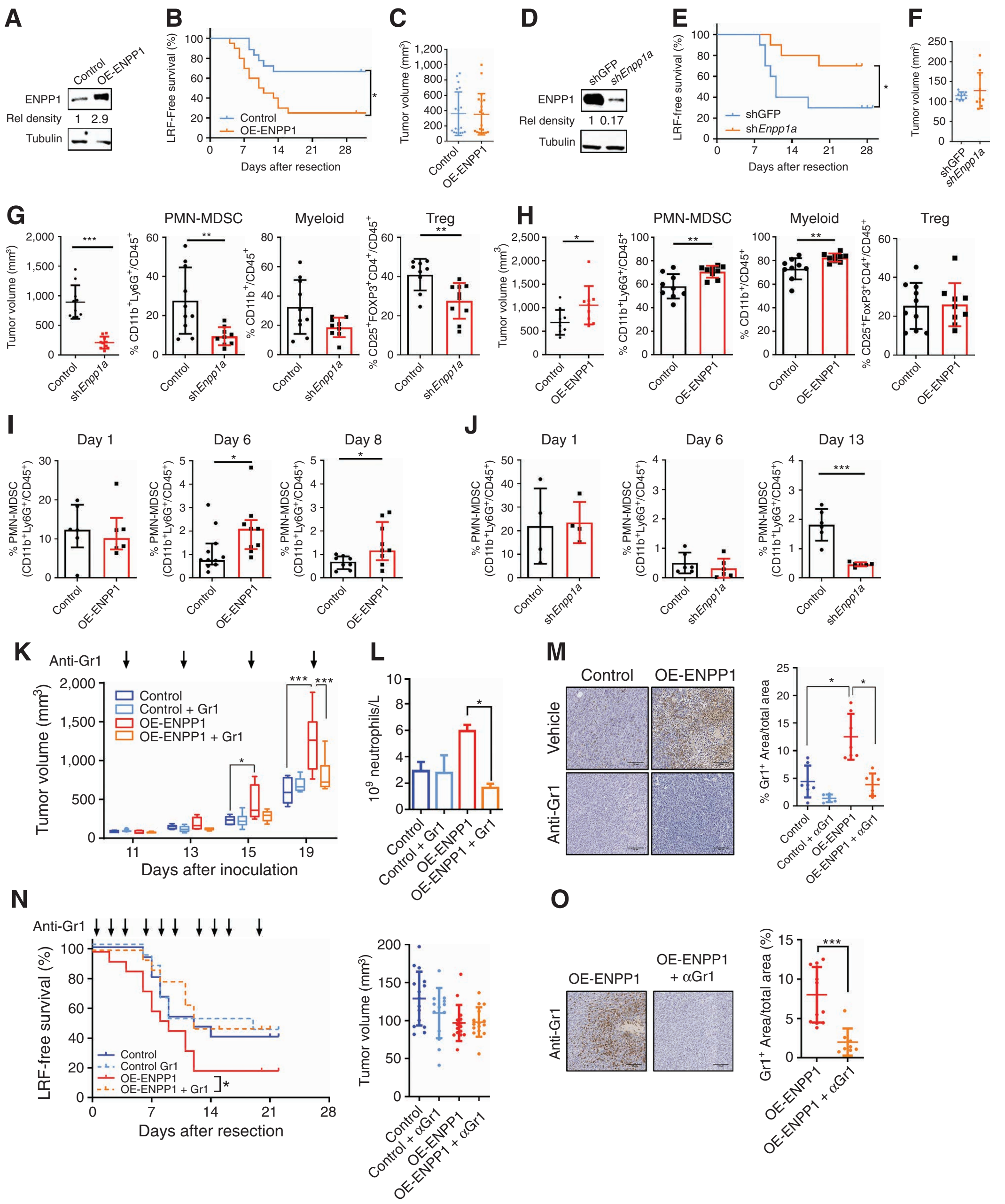

**Figure 3.** ENPP1 levels modulate tumor–immune landscape and mediate LRF. LRF was assessed in tumors derived from cells expressing different levels of ENPP1. **A,** Western blot analysis of ENPP1 protein levels in control (ANV5-mock) and cells overexpressing ENPP1 (OE-ENPP1). **B,** Kaplan–Meier curve of the LRF rate in mice inoculated with control and OE-ENPP1 cells ($n = 18$ mice per group). No differences in tumor margins between groups were detected. **C,** Tumor volume at day of surgery for each mouse. **D,** Western blot analysis of lentivirally silenced 720Cy2Rx cells with a shGFP control and silenced with sh*Enpp1* (sh*Enpp1a*). **E,** LRF-free survival curves with 10 mice per group. No differences in tumor margins between groups were detected. **F,** Tumor volume at day of surgery is represented for each mouse. **G,** Tumor volume at the day of resection from orthotopic injected tumor cells (left) and flow-cytometric quantification by CytoFLEX of tumor-infiltrating immune subpopulations derived from orthotopic tumors of control (720Cy2Rx) and sh*Enpp1a* cells. **H,** Similar quantification as in **G** in orthotopic tumors derived from control (ANV5-mock) and OE-ENPP1 cells. **I,** Time-course analysis by flow cytometry of PMN-MDSC infiltration after orthotopic injection of OE-ENPP1 cells and controls at the indicated times post-injection ($n = 8$ mice per group). Student *t* test was used for comparison. **J,** Similar experiment as in **I** with sh*Enpp1a* cells and controls (shGFP). PMN-MDSC infiltration in orthotopic tumors ($n = 8$ mice per group) injected with control or shEnpp1a cells. Student *t* test was used for comparison. **K,** Orthotopic tumor volume of tumors derived from OE-ENPP1 and control ANV5 cells in animals ($n = 8$ mice/group) treated with vehicle or anti-Gr1 antibody (200 μg/mouse/ injection) at the indicated frequency (arrows). Kruskal–Wallis was used for comparison. Median and interquartile range is represented. **L,** Blood neutrophil counts on day of sacrifice. **M,** Representative images of anti-Gr1⁺ immunostaining of the indicated tumors. Quantification of Gr1⁺ cells was performed by ImageJ. One-way ANOVA was used for comparison. Scale bar, 100 μm. **N,** LRF-free survival after tumor resection of mice orthotopically inoculated with OE-ENPP1 cells or control cells and treated with vehicle or anti-Gr1⁺ antibody three times per week (arrows). Control groups: 15 mice/group and $n = 30$/group for OE-ENPP1 groups. Tumor volume at surgery is represented in the right-hand plot. No differences in tumor margins between groups were detected ($\chi^2$ test). **O,** Representative images of relapsed tumors (left) and quantification (right) of Gr1⁺ immunostaining of the indicated tumors. Student *t* test; scale bar, 100 μm. Log-rank test was used in Kaplan–Meier plots. *, $P < 0.05$; **, $P < 0.01$; ***, $P < 0.0001$.

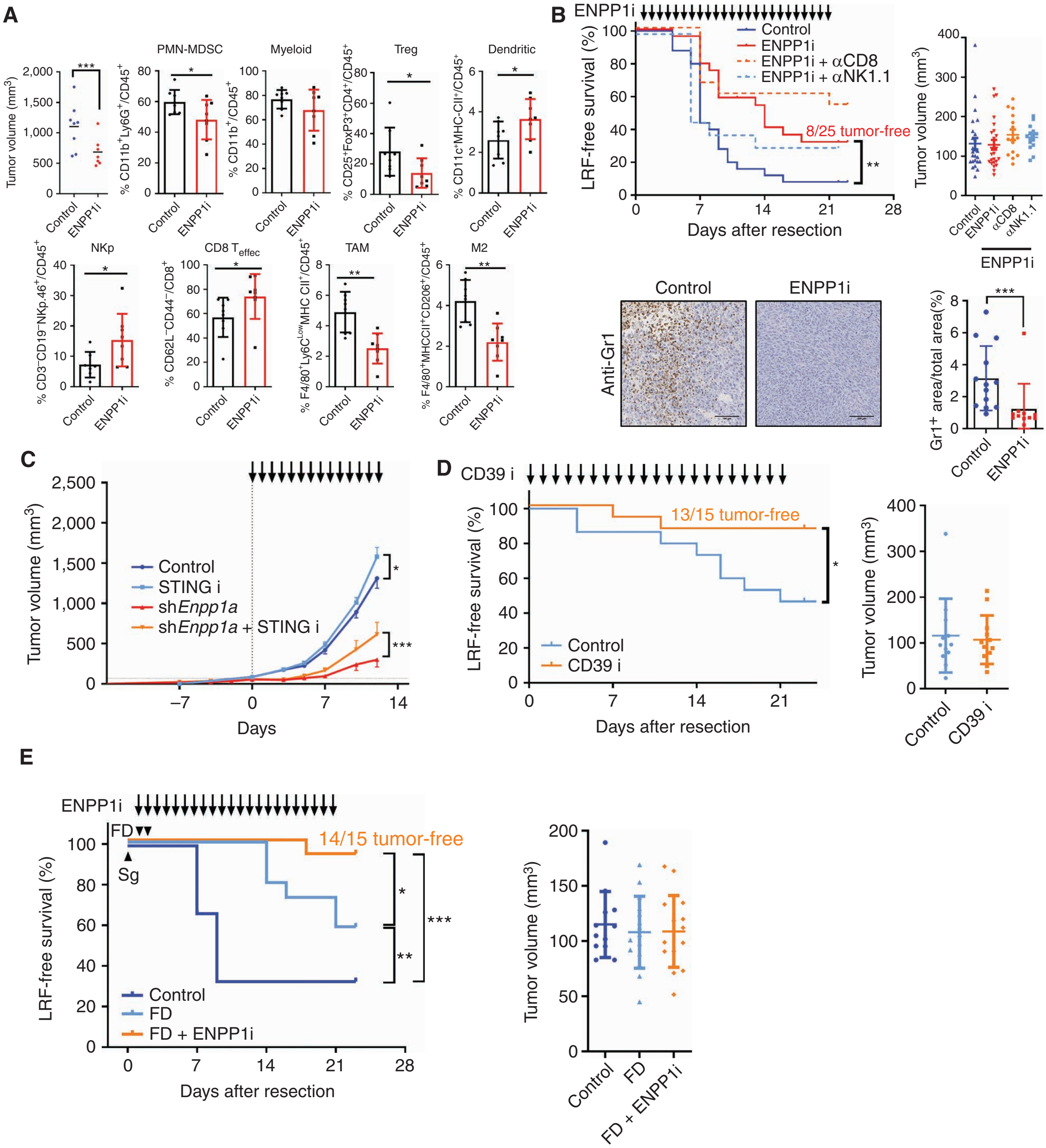

**Figure 4.** Functional role of the ENPP1i in immune remodeling. **A,** Tumor volume at the day of resection after orthotopic inoculation of OE-ENPP1 cells. Mice ($n = 8$ mice/group) were treated daily with ENPP1i (CM3163) or vehicle. Flow-cytometric quantification of tumor-infiltrating immune subpopulations. **B,** LRF-free survival of two groups of mice ($n = 25$ mice/group) previously inoculated with 720Cy2Rx cells were treated daily (arrows) after tumor resection with the ENPP1i (CM3163) alone or with anti-CD8, anti-NK1.1–depleting antibodies (200 ug of antibodies 3 times per week), or vehicle. Right, tumors were resected at the indicated sizes. Tumor recurrence was detected by palpation and verified by histologic analysis. No differences in tumor margins between groups were detected. Bottom left, representative images of immunostaining of tumors (scale bar, 100 μm). Bottom right, quantification of IHC images of Gr1+ cells in all relapsed tumors using a blinded automated system based on ImageJ. Student *t* test. **C,** Tumor volume of tumor derived from orthotopic implantation of control (shGFP-720Cy2Rx) or sh*Enpp1a* cells treated with the STING inhibitor (arrows; C-176, 5 mg/kg i.p. daily; $n = 15$ mice per group). Two-way ANOVA was applied. Mean ± SEM are represented. **D,** LRF-free survival after the surgical resection of tumors derived from sh*Enpp1* cells. After tumor resection, animals ($n = 15$ per group) were treated daily with the CD39 inhibitor (POM-1, 5 mg/kg) or vehicle control (arrows). Right, tumors were resected at the indicated sizes. **E,** LRF-free survival after tumor resection from OE-ENPP1–implanted cells. Mice ($n = 15$ mice per group) were treated with FD (4 doses of 6.2 Gy) irradiation on two consecutive days after surgery (sg), or in combination with the Enpp1i daily (arrows) at 50 mg/kg subcutaneously or sham-operated and treated with vehicle (control). Right, tumor volume at the day of surgery in each group. No differences in tumor margins between groups were detected. Log-rank test was used in Kaplan–Meier curves. *, $P < 0.05$; **, $P < 0.01$; ***, $P < 0.0001$.

treatment was used with or without IR after surgical resection of tumors. As expected, FD treatment improved the LRF-free survival as compared with the non-IR group. Interestingly, FD treatment with ENPP1i further extended the LRF-free survival, reaching a remarkable improvement in local control, and resulted in only 1 of 15 mice with LRF (Fig. 4E). Thus, these findings indicate that the combination of IR with ENPP1i reached a superior benefit in terms of obliterating LRF.

## ENPP1$^{hi}$ Tumor Cells Mobilize PMN-MDSC through HP

Next, we tested whether tumor cells with different ENPP1 levels could differently modulate PMN-MDSC migration and function. Murine PMN-MDSC were purified from the spleen of tumor-bearing mice, reaching 97% purity. We also obtained PMN-MDSC differentiated from murine bone marrow after *ex vivo* culture, reaching 60% purity. In both cases, flow cytometry analysis revealed the expression of C–C chemokine receptor type 2 (CCR2), also reportedly expressed on human neutrophils (ref. 26; Supplementary Fig. S8A and Methods). Using a Boyden chamber assay, we observed a significant increase in the migration/invasion of PMN-MDSC placed in the upper compartment when incubated with OE-ENPP1 ANV5 tumor cells in the lower chamber. This effect was abrogated with an ENPP1i. Consistently, PMN-MDSC had a significant decrease in chemoattraction when *Enpp1*-silenced 720Cy2Rx cells (sh*Enpp1a* and sh*Enpp1b*) were placed in the lower chamber as compared with control cells, suggesting a chemotactic effect associated with ENPP1 levels (Fig. 5A).

To identify mediators of this ENPP1-dependent effect on MDSC invasiveness, we performed RNA-seq in OE-ENPP1 versus control in ANV5 and 4T1 cells. We selected 146 common differentially overexpressed genes that were coherent between cell lines with $P < 0.05$ and log-fold change >0. A similar approach was used to identify downregulated genes in two *Enpp1*-silenced cells (720Cy2Rx and 374Cy2NoRx cells) with two independent shRNAs (Fig. 5B). By crossing upregulated genes in OE-ENPP1 cell lines with downregulated genes in silenced cell lines, we identified a coherent 16-gene signature associated with ENPP1 levels (Fig. 5B). The most significant gene associated with ENPP1 levels was *Hp*, an acute secreted inflammatory component known for binding free hemoglobin (Fig. 5C).

Consistent with ENPP1 levels, HP expression levels were validated in cell lysates (Supplementary Fig. S8B) and in the conditioned media (CM; Fig. 5D). HP expression was also diminished when cells were incubated with ENPP1i (Supplementary Fig. S8C), indicating an ENPP1-mediated comodulation of HP levels. Based on these findings, we reasoned that a mechanistic link between ENPP1 and HP could be mediated by ENPP1 activity or its product metabolites as a result of the adenosinergic pathway. As ADO is the common downstream metabolite to the noncanonical and canonical pathways, we postulated that high levels of ADO could mediate the coregulation of HP. As ADO stimulates intracellular cyclic AMP levels through Gs-coupled P1 receptor subtypes A2AR and A2BR, we used forskolin, an activator of adenylyl cyclase, or 8-Br-cAMP, as cAMP mimetics. Incubation strongly induced HP secretion in the CM of ANV5 (Fig. 5E). Secretion was inhibited by coincubation with a competitive antagonist of P1 receptors (SCH-58261). Moreover, NECA (5′-N-ethylcarboxamidoadenosine), a nonselective ADO receptor agonist, also stimulated HP secretion, and this effect was markedly reduced by the ADO receptor antagonist. In *Enpp1*-silenced cells, HP levels were rescued upon agonist stimulation, and these effects were reduced by coincubation with the ADO receptor antagonist (Fig. 5E). Similar effects were observed in 4T1 cells and its derivative (Supplementary Fig. S8D). Concordant with ENPP1 effects, purified HP per se increased the migration chemotactic index (MCI) of murine PMN-MDSC in a dose-dependent manner, an effect abrogated by the use of a CCR2 inhibitor (RS-102895; Fig. 5F). Furthermore, CM of *Hp*-silenced cells led to diminished MCI of PMN-MDSC cells (Fig. 5G). CM of ANV5 parental cells treated with cAMP mimetics or the ADO receptor agonist increased the MCI of myeloid cells, effects that were abrogated by coincubation with a P1 receptor antagonist

**Figure 5.** Mechanistic modulation of myeloid chemotactic migration by HP. **A,** Chemotactic migration was assessed in Boyden chambers for 24 hours after seeding murine bone marrow–derived PMN cells differentiated *in vitro* in the upper chamber and the indicated cells in the bottom compartment. Negative control: no cells with serum-free medium (C–). Positive control: no cells with complete medium (C+). OE-ENPP1 cells were seeded alone or incubated with 5 μmol/L of the ENPP1i (CM3163); control cells (720Cy2Rx, which express high ENPP1 levels) and two different shRNAs silencing *Enpp1*. Student *t* test was used. Error bars, mean ± SEM; $n = 4$ different biological replicates; data are representative of four independent experiments with similar results. **B,** Strategy for the transcriptomic analysis by RNA-seq was performed in triplicate for all represented cell lines. Venn diagram showing overlap of regulated genes with log-fold change >0 and $P < 0.05$. Top left, 4T1 and OE-4T1 and ANV5 and OE-ANV5. Bottom left, 720shControl with 720sh*Enpp1a* and *b* and 374shControl with 374sh*Enpp1a* and *b*. Right, Venn diagram showing coherent and significant upregulated genes in OE-ENPP1 with downregulated genes in sh*Enpp1* from previous analyses yield 16 significant genes. **C,** Hierarchical clustering of significant 16-gene signature. *Hp* is highlighted in red. **D,** Top, Western blot analysis of HP in the four-day secretome of cells with different levels of ENPP1. CM obtained in serum-free conditions after concentration (×150) was normalized using 20 μg of protein per lane. Bottom, ENPP1 levels in cell lysates. Relative expression is represented from densitometric quantification. Bold numbers are arbitrary units. **E,** Left, scheme of the Gs-coupled P1 receptors subtypes (A2AR and A2BR), showing the receptor antagonist (SCH-58261). NECA was used as a stable P1 receptor agonist and two downstream cAMP mimetics. Western blot analysis of HP obtained after incubation with forskolin, 8-Br-cAMP, and NECA with or without the P1 inhibitor (7 μmol/L) in ANV5 and its derivative 720sh*Enpp1a* cell line. Numbers represent the densitometric normalization of the signal in triplicate experiments. Serum-free CM cells obtained after four days of incubation were concentrated (×150) and normalized using 20 μg of protein per lane. **F,** Boyden chamber evaluation of chemotactic migration index (MCI) of murine bone marrow–derived PMN-MDSC induced by increasing doses of HP (0.02, 0.1, and 0.5 mg/mL) in serum-free media for 24 hours. CCR2 inhibitor (RS-102895) was added at 10 μmol/L in coincubation with HP (0.5 mg/mL). C, Control: serum-free medium. One-way ANOVA was used. Mean ± SD. CXCL2 (100 ng/mL) was a positive chemotactic control was used alone (–) or coincubated with the CCR2 inhibitor (10 μmol/L). **G,** MCI of murine bone marrow–derived PMN cells (upper chamber) induced by CM (bottom) in Boyden chambers obtained from the indicated cells after four days of incubation. Top, Western blot of the CM derived from the indicated cells transduced with two different shRNAs targeting *Hp*. Left, control (720Cy2Rx) and *Hp*-silenced cells. Right, CM derived from ANV5 cells alone or stimulated with the cAMP (Forskolin, 8-Br-AMP), or ADO mimetics (NECA) alone or in combination with the P1 inhibitor. CM was diluted with fresh medium (1:1) for the assay. One-way ANOVA was used. *, $P < 0.05$; **, $P < 0.01$; ***, $P < 0.001$.

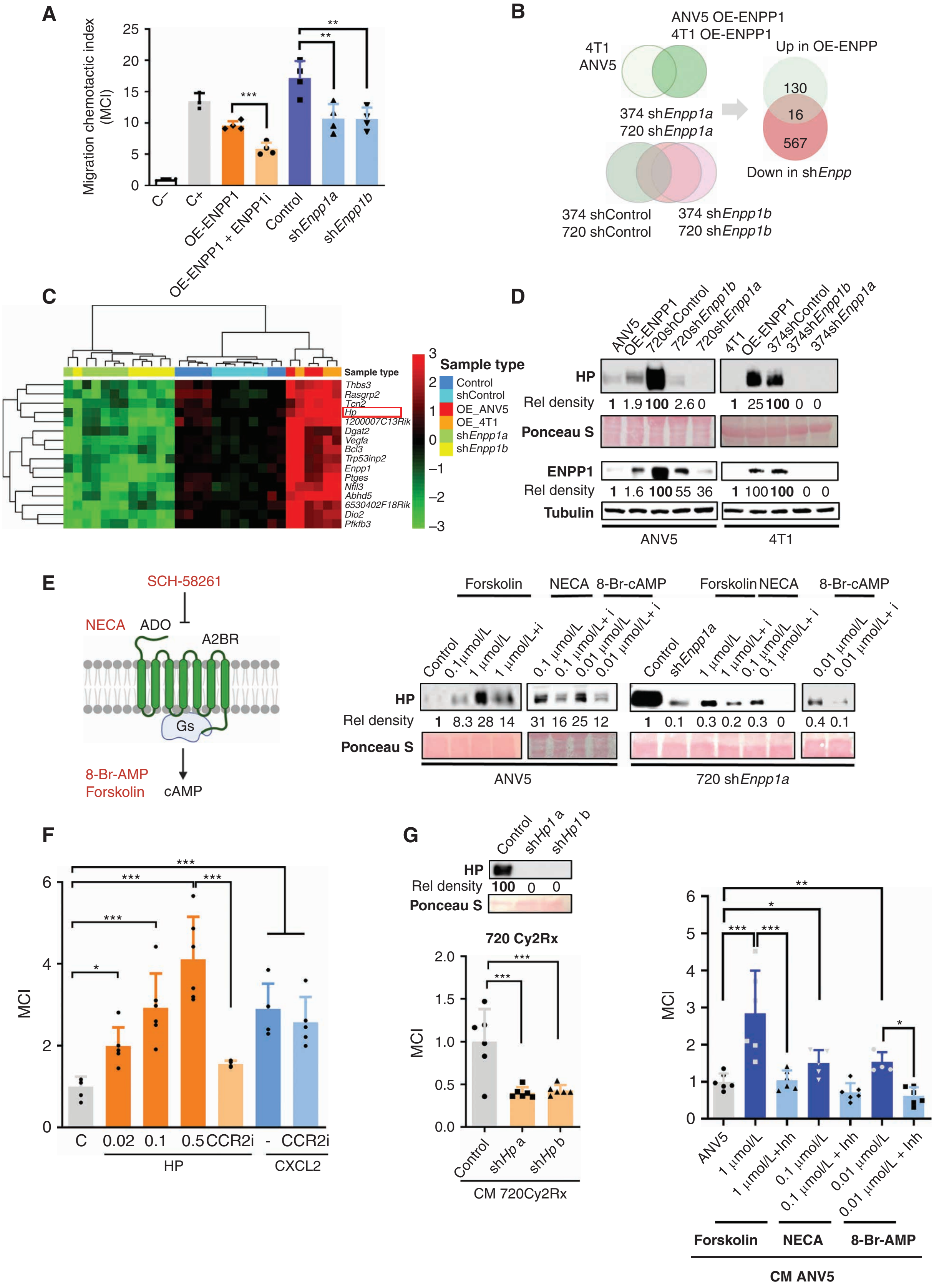
A
Migration chemotactic index (MCI)
25
20
15
10
5
0
C−
C+
OE-ENPP1
OE-ENPP1 + ENPP1i
Control
shEnpp1a
shEnpp1b
***
**
**
B
4T1
ANV5
ANV5 OE-ENPP1
4T1 OE-ENPP1
374 shEnpp1a
720 shEnpp1a
374 shControl
720 shControl
374 shEnpp1b
720 shEnpp1b
Up in OE-ENPP
130
16
567
Down in shEnpp
C
Sample type
Thbs3
Rasgrp2
Tcn2
Hp
1200007C13Rik
Dgat2
Vegfa
Bcl3
Trp53inp2
Enpp1
Ptges
Nfil3
Abhd5
6530402F18Rik
Dio2
Pfkfb3
3
2
1
0
−1
−2
−3
Sample type
Control
shControl
OE_ANV5
OE_4T1
shEnpp1a
shEnpp1b
D
ANV5
OE-ENPP1
720shControl
720shEnpp1b
720shEnpp1a
4T1
OE-ENPP1
374shControl
374shEnpp1b
374shEnpp1a
HP
Rel density
1 1.9 100 2.6 0
1 25 100 0 0
Ponceau S
ENPP1
Rel density
1 1.6 100 55 36
1 100 100 0 0
Tubulin
ANV5
4T1
E
SCH-58261
NECA
ADO
A2BR
Gs
8-Br-AMP
Forskolin
cAMP
Forskolin
NECA
8-Br-cAMP
Forskolin
NECA
8-Br-cAMP
Control
0.1 µmol/L
1 µmol/L
1 µmol/L+i
0.1 µmol/L
0.1 µmol/L+ i
0.01 µmol/L
0.01 µmol/L+ i
Control
shEnpp1a
1 µmol/L
1 µmol/L+ i
0.1 µmol/L
0.1 µmol/L+ i
0.01 µmol/L
0.01 µmol/L+ i
HP
Rel density
1 8.3 28 14
31 16 25 12
1 0.1 0.3 0.2 0.3 0
0.4 0.1
Ponceau S
ANV5
720 shEnpp1a
F
MCI
6
4
2
0
***
***
***
***
*
C
0.02
0.1
0.5
CCR2i
-
CCR2i
HP
CXCL2
G
Control
shHp1a
shHp1b
HP
Rel density
100 0 0
Ponceau S
720 Cy2Rx
MCI
2.0
1.5
1.0
0.5
0.0
***
***
Control
shHp a
shHp b
CM 720Cy2Rx
MCI
6
5
4
3
2
1
0
**
*
***
***
*
ANV5
1 µmol/L
1 µmol/L+Inh
0.1 µmol/L
0.1 µmol/L + Inh
0.01 µmol/L
0.01 µmol/L + Inh
Forskolin
NECA
8-Br-AMP
CM ANV5

(Fig. 5G). Similar results were obtained in 4T1 cells (Supplementary Fig. S8E). These findings indicate that the ENPP1 hydrolysis product AMP, and its derivative, ADO, stimulate the secretion of HP to the extracellular milieu in breast cancer cell lines, an effect mediated by purinergic P1 receptors. In turn, HP induces the migration and invasion of PMN-MDSC *in vitro*, an effect mediated by CCR2.

### Secreted HP Promotes NET Formation

As other proinflammatory factors such as C5a (a downstream effector of complement activation) are strong inducers of NET formation, an extrusion primarily composed of DNA complexed with proteins, we inquired whether HP as an acute phase component could also promote NET formation. As expected, a significant number of NET were observed with C5a, as compared with unstimulated cells (Supplementary Fig. S8F). Interestingly, upon incubation with HP, we observed prominent NET formation, a process that was again strongly diminished by the NET inhibitor, PAD4 inhibitor, and using 720Cy2Rx cells with *Hp*-silenced levels (Fig. 6A and B).

Based on this finding, we also investigated the ability of PMN-MDSC to induce NET formation *in vitro* upon incubation with tumor cells with different ENPP1 levels. To test this, ANV5 cells were cocultured with mouse PMN-MDSC. Interestingly, OE-ENPP1 tumor cells showed a significant induction of NET that was further abrogated with an ENPP1i and A2ARi (SCH-58261; Fig. 6C and D). Similarly, silenced levels of *Enpp1* led to a significant decrease in NET formation. Taken together, these findings indicate that tumor ENPP1 levels differentially modulate neutrophil chemotactic invasiveness and NET formation *in vitro*. To further substantiate these findings, we assessed the relevance of HP in LRF; mice inoculated with *Hp*-silenced cells showed an almost significant improvement in LRF-free survival as compared with control mice ($P = 0.07$). Of note, tumor volume and resection margins at surgery were significantly different between groups (Supplementary Fig. S8G), suggesting that HP might be an important component involved in LRF possibly mediating NET formation *in vivo*. More importantly, LRF of animals treated with NET inhibitors (PAD4i or DNase) improved LRF-free survival rate, indicating that abrogation of NET formation strongly influences relapse-free survival (Fig. 6E).

### Clinical Relevance of ENPP1 and NET in LRF

To investigate the clinical relevance of the identified LRF gene signature, we used the *in silico* tool Kaplan–Meier plotter in a cohort of patients with TNBC. Patients were segregated according to the computed gene-expression levels. Patients with TNBC with high levels of *ENPP1* had significantly shorter recurrence-free survival (RFS; $P = 0.0011$; Fig. 7A). Interestingly, in a cohort of 405 patients with TNBC, high levels of *HP* were associated with a diminished RFS ($P = 0.0093$; Fig. 7A). In contrast, gene-expression levels of other components of the LRF signature did not show the expected correlation with RFS in those patients (Supplementary Fig. S9A). Of note, copy number of *ENPP1* is frequently amplified in breast cancer cohorts (Supplementary Fig. S9B).

To further study this association, we constructed a breast cancer tissue microarray (TMA) containing 54 paired specimens from 27 HER2$^+$ and TNBC patients with primary breast cancer who developed LRF (Supplementary Table S4). IHC analysis of ENPP1 in a TMA of primary versus recurrent breast cancer human tumors obtained from the same patient showed a significant increase of ENPP1 in recurrent tumors as compared with that in paired primary tumors ($P = 0.0324$; Fig. 7B).

Furthermore, we evaluated the density occupied by NETs in the same human cohort including naïve primary tumors and relapsed tumors post-surgery and post-IR. Interestingly, the NET-occupied area, identified by costaining with CD15, myeloperoxidase (MPO), and citrullinated histone H3 (H3Cit), was significantly increased in relapsed tumors as compared with their respective primary tumor NET levels at diagnosis ($P = 0.013$; Fig. 7C–E). Of note, the density of neutrophil infiltration correlated with the area of NET, possibly indicating a relationship between neutrophil tumor infiltration and NETosis.

## DISCUSSION

LRF post-surgery and post-radiotherapy poses a major challenge in the management of patients with breast cancer. By modeling this event, we demonstrate a conserved mechanism by which ENPP1$^{hi}$ CTC are endowed with increased fitness for homing and colonization of the recurrent tumor bed and subsequent tumor relapse, in part for their ability to recruit PMN-MDSC. Infiltration by this immunosuppressive myeloid subpopulation is enabled by ENPP1 hydrolysis metabolites acting in an autocrine/paracrine loop to trigger HP tumor secretion. Interestingly, its chemoattractant activity promotes this myeloid intrusion and generates robust NET formation. Accordingly, blocking ENPP1 or NET formation or eradicating engrafted CTC by IR diminishes CTC colonization, leading to a reduction in the LRF rate. The most salient finding was an almost complete LRF abrogation after ENPP1 blockade was added to standard fractionated IR post-surgery. This synergism is substantiated by the antitumor immune response elicited by ENPP1i acting in the immune infiltrate, its tumor radiosensitizing effect, and by the more radiosensitive immune infiltrate by eradicating neutrophil infiltration and NET formation (27, 28). Beyond the cytotoxic effect of FD, the number of residual cells and intervals between fractions may affect LRF (6). FD has also shown a significant antitumor benefit leading to the production of IFNβ required for the function of dendritic cells, which in turn primed tumor-specific CD8$^+$ T cells, boosting immune-mediated antitumor responses and synergizing with checkpoint inhibitors (29). These results underscore the potential of this combination to boost current therapeutic options in post-surgical IR and strongly substantiates a proof-of-concept for the future development of clinical trials.

This report highlights a unique role of ENPP1 in tumor relapse, specifically in CTC colonizing the RTB. ENPP1 confers further advantages during early events of recurrence, in which ENPP1$^{hi}$ cells are more prone for efficient engraftment, survival, and growth in the RTB.

This ENPP1$^{hi}$ CTC phenotype arose independently of IR and conferred an increased fitness for secondary outgrowths

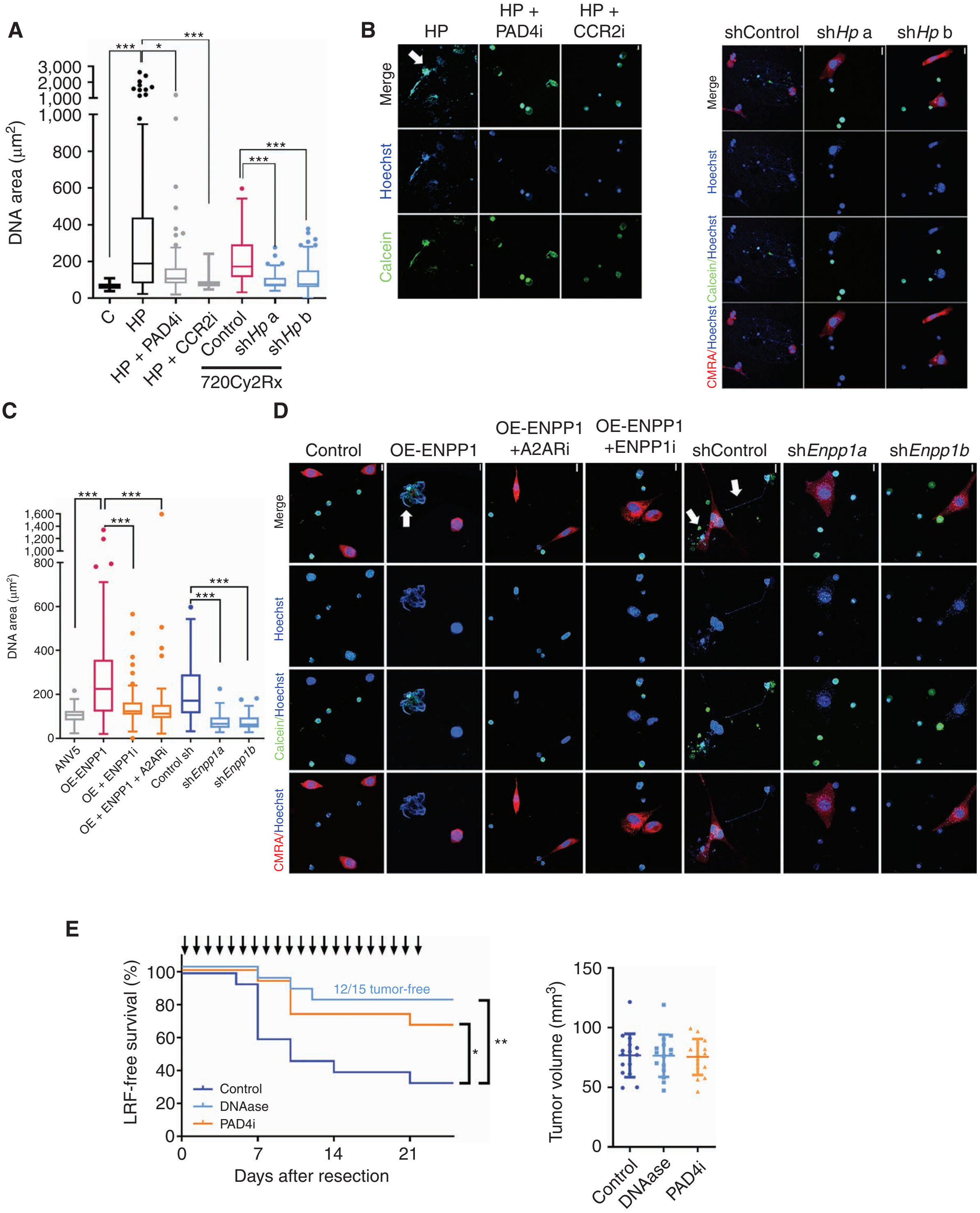

**Figure 6.** ENPP1 and HP modulate NET formation. **A,** Quantification of the DNA area of NET induced by HP incubation (0.5 mg/mL) in serum-free media for 48 hours or coincubated with the NET inhibitor (PAD4i) or CCR2 inhibitor. Serum-free media were used as control (C). NET formation was quantified in the presence of control (shGFP) or *Hp*-silenced cells (sh*Hp* a and b). Kruskal–Wallis test was applied. **B,** Representative fluorescent images of PMN-MDSC (green) and nuclei were stained with Hoechst. Arrows indicate NET. PAD4i and CCR2i were used to block NET formation. **C,** Quantification of fluorescent images of the DNA area of NET in the presence of the indicated tumor cells overexpressing ENPP1 (OE-ENPP1) or with silenced levels (sh*Enpp1*a and *b*) incubated with vehicle or with an ENPP1i (CM3163) at 5 µmol/L or an A2AR inhibitor (SCH58261) at 5 µmol/L. Kruskal–Wallis test was used for comparison. **D,** Representative fluorescent images of cocultured tumor cells (red) with PMN-MDSC (green). Nuclei were stained with Hoechst. Arrows point to NET. Scale bar, 10 µm, as shown in the top corners. **E,** LRF-free survival rate in mice inoculated with 720Cy2Rx cells treated with vehicle or two NET inhibitors (arrows; DNase I, 2.5 mg/kg or PAD4i, GSK484, 5 mg/kg) daily from tumor resection ($n = 15$ mice per group). Log-rank test; *, $P < 0.05$; **, $P < 0.01$; ***, $P < 0.001$. Right, tumor volume at resection.

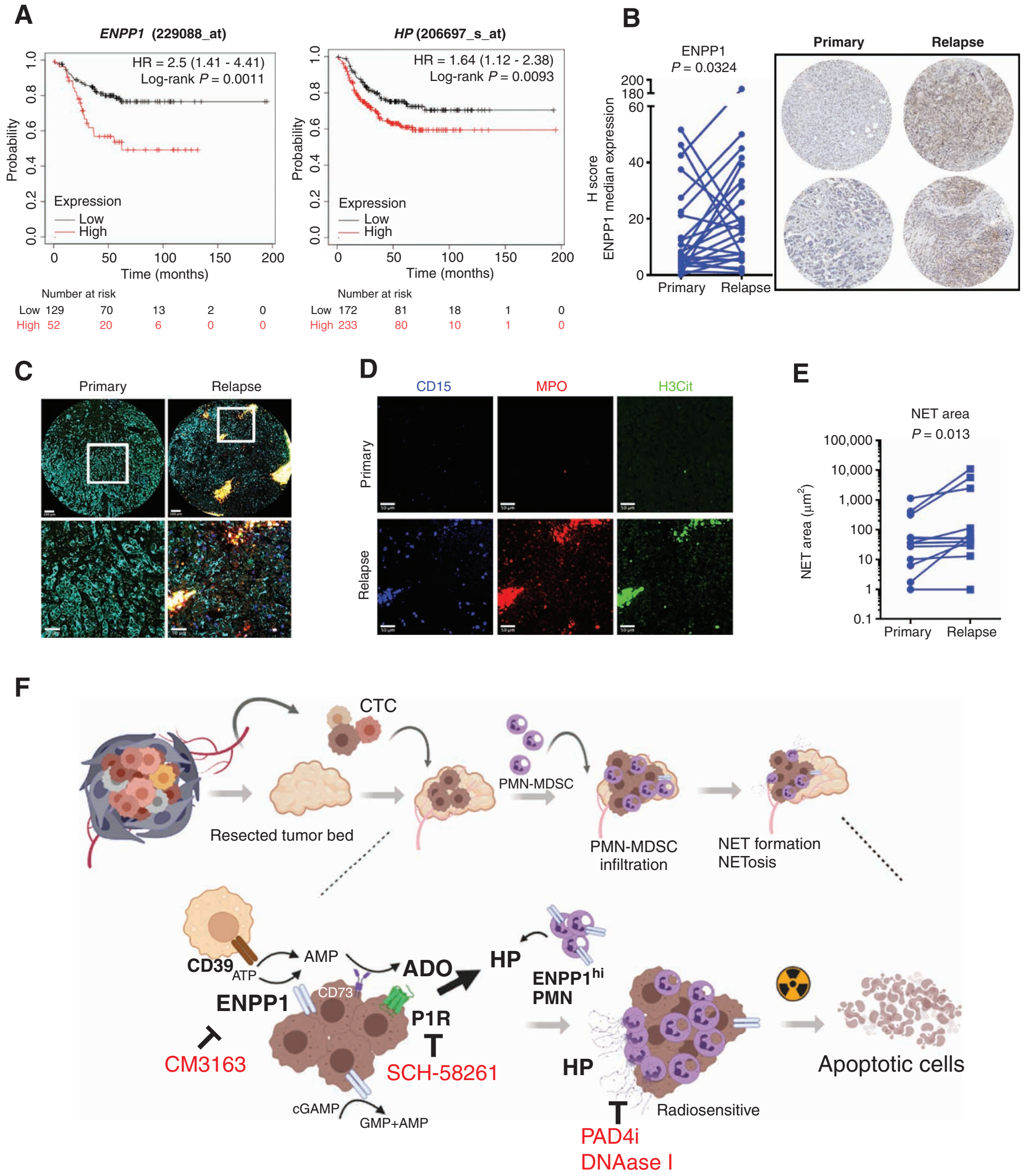

**Figure 7.** ENPP1 and NET in human TNBC. **A,** *In silico* analysis of the prognostic value of gene-expression levels using the Kaplan–Meier plotter (www.kmplot.com) of *ENPP1* (Affy ID: 229088_at) and *HP* (Affy ID: 206697_s_at) in TNBC. Differences between groups were evaluated using the log-rank test. **B,** Left, quantification of ENPP1 immunostaining in a TMA of human breast cancer primary and relapsed breast tumors. Nonparametric Wilcoxon paired sample test was used for comparison. Right, representative images. **C,** Representative images of NET evaluation by multispectral imaging with an automated quantitative pathology imaging system (Vectra Polaris) in primary nontreated breast cancer tumors and their paired relapsed TNBC tumors from formalin-fixed, paraffin-embedded tissue sections of a TMA. Representative composite images immunostained with CD15 (clone Carb-3, blue), MPO (clone C8/144B, red), anticitrullinated histone (H3Cit; green, citrulline R2 + R8 + R17), cytokeratin (wide spectrum screening, cyan), and DAPI (gray). NET are costained with CD15, MPO, and H3Cit. NET are visualized as white structures in the full composite color images. Square is magnified in the bottom plots. Top: scale bar, 100 μm. Bottom: scale bar, 50 μm. **D,** Segmented fluorescence images for CD15, MPO, and H3Cit for magnified squares shown in **C**, showing coimmune localization of three markers, indicating *bona fide* NET. Scale bar, 50 μm. **E,** Quantification of the NET area of the multispectral images obtained. Nonparametric Wilcoxon paired sample test was used for comparison. **F,** Schematic of the mechanism of LRF at the cellular and molecular levels. Top, primary breast tumors release CTC. After surgery, the RTB constitutes a fertile soil for CTC. ENPP1$^{\text{hi}}$ CTC are more competent to engraft and efficiently colonize the RTB. ENPP1$^{\text{hi}}$ cells promote the intrusion of PMN-MDSC and strong immunosuppressed microenvironment in the recurrent tumor. PMN-MDSC create NET, which also abolish the immune attack. Bottom, at the molecular level, ENPP1 hydrolyzes ATP into AMP and pyrophosphate (PPi). Similarly, CD39 in the microenvironment hydrolyzes ATP to AMP. AMP is hydrolyzed to adenosine (ADO) by CD73 in the adenosinergic pathway (CD39–CD73). The accumulation of AMP in the TME induces the secretion of HP through P1 purinergic receptors. HP and other components act as chemoattractant factors for PMN-MDSC that infiltrate and contribute to the incipient tumor colonization by an immunosuppressive TME from early stages of tumor formation. This also leads to immune landscape remodeling by impairing NK and CD8$^{+}$ T-cell infiltration. Secretion of HP also induces NET formation, which further promotes an immunosuppressive microenvironment. Radiation obliterates the early engraftment of CTC. ENPP1 inhibition decreases the extracellular AMP and ADO levels and decreases HP with an enhancement of an immunocompetent microenvironment. ENPP1 blockade radiosensitizes the tumor, triggers the infiltration of CD8 and NK, and decreases the infiltration of Tregs and myeloid suppressor cells. In this scenario, tumor cells are less competent to colonize the RTB. Subsequent fractionated irradiation contributes to eradicate engrafted tumor cells, preventing locoregional failure, but does not prevent the subsequent homing of CTC post-IR.

in the RTB. Tumor-intrinsic factors leading to ENPP1$^{hi}$ phenotype are unknown but could be prompted by tumor–stromal interactions or other contextual factors of the tumor milieu at the primary tumor and can be further enriched during relapse. Of note, a strong ENPP1 expression signal was also detected in the stromal compartment of some infiltrating breast cancer tumors, indicating a potential tumor–stromal cross-talk (30).

Several mechanisms were also unpredictably exploited by ENPP1$^{hi}$ tumor cells to mediate LRF. First, ENPP1 levels were unexpectedly comodulated with the tumor-secreted HP. This protein is a well-known component of the acute inflammatory response, aside from its ability to sequester free hemoglobin released into the bloodstream to prevent hemoglobin-induced oxidative damage (31). This previously uncovered association links its proinflammatory function with the antitumor immune response and posits the ENPP1/HP axis as a new mechanism by which tumor cells subdue myeloid cells to boost LRF. We showed that AMP by an autocrine/paracrine signaling via ADO receptors in the tumor strongly stimulated HP secretion, establishing a mechanistic link between ENPP1 and HP through purinergic P1 receptors. ADO is also increased by IR, which also upregulates other ADO-generating enzymes such as CD38 (32, 33). ADO levels are also dependent on the activity of the CD39/CD73 pathway expressed by cancer cells, immune cells, and the vasculature. Indeed, CD39 blockade in ENPP1-silenced cells led to a significant reduction in the LRF rate, indicating that a blockade of the remnant activation of the adenosinergic pathway, especially in immune-infiltrating cells, could be necessary to reach a more salient effect. Although this point requires further investigation, several clinical trials targeting CD73/ADO receptors are currently ongoing.

Besides its role in the adenosinergic pathway, tumor ENPP1 also hydrolyzes the extracellular cGAMP, a danger signal of the STING pathway, to AMP and GMP, and this degradation prevents detection by the immune system. We cannot discard the possibility that other extracellular purines or pyrimidines in the TME could also stimulate tumor HP. Moreover, IR could exacerbate these findings as this treatment augments extracellular cGAMP. Importantly, accumulation of cGAMP by ENPP1 inhibition activates the cGAS–STING pathway, leading to an antitumor immune attack, which was reversed using a STING inhibitor, resulting in tumor growth in ENPP1-silenced cells. Indeed, STING activation in noncancer cells leads to increased numbers of cross-presenting dendritic cells and subsequent T-cell activation and NK-cell responses (34). Similarly, ENPP1i treatment led to an increased tumor-associated dendritic CD11c$^{+}$ MHC-CII$^{+}$ population and NK infiltration. Although cGAS–STING activation by emerging agonists could reduce tumor relapse, we could anticipate that concurrent ENPP1 blockade could reach more noticeable antitumor effects because ENPP1i boosted a strong immune landscape remodeling with an additional reduction of myeloid cells.

Of note, ENPP1 inhibition was more pronounced than ENPP1-silencing effects, as it may also affect most of the immune subpopulations expressing ENPP1 (35). Our findings were also in line with previous studies showing that PMN-MDSC inhibit the activity and function of other myeloid subpopulations and NK cells (36). Consequently, ENPP1 levels were associated with poor prognosis in a subset of patients with breast cancer. These observations support the potential benefit of combining immune-checkpoint inhibitors with ENPP1 inhibition to obtain a superior antitumor immune response.

Second, HP released in the inflammatory milieu constitutes a novel factor orchestrating myeloid infiltration and NET formation. This dual function exerted by HP on PMN-MDSC might be dependent on its concentration gradient and the duration of the stimulus, as myeloid intrusion predates NET formation (37). HP-induced myeloid migration was supported by early observations where HP-specific binding to neutrophils was shown to modulate effector functions (38) and subsequent findings (26). However, we cannot discard the possibility of a more complex interaction between HP and PMN-MDSC that may involve other unidentified players. The PMN-MDSC infiltration kinetics detected from incipient nonpalpable tumors indicated a sustained effect (Fig. 3I and J). Interestingly, NET formation was required for LRF because its abrogation was associated with a significantly better LRF-free survival, underscoring a novel role of NET formation in LRF. It is tempting to speculate that NET could participate in the accumulated trapping of CTC in the RTB, further increasing the LRF rate, and eventually initiate the development of secondary outgrowths at local or distant locations (Fig. 7F). Reportedly, NET participate in the capture of metastatic emboli during colonization (39). Furthermore, NET could also interfere with antitumor immune cytotoxicity, creating a tumor-protective shielding mechanism (40). As NET formation also primed the premetastatic niche and promoted tumor dissemination in a lung metastasis model of breast cancer (41), inhibition of NET hampered the progression of established tumors and impaired metastasis (40). Concordantly, an increased NET area was detected in relapsed breast cancer specimens in our cohort (42). Thus, we could anticipate that several NET inhibitors currently tested in the clinic, including PAD4 antagonists, IL8-neutralizing antibodies (43), and CXCR2 inhibitors, could also affect LRF. Similarly, given the central role of ENPP1 in myeloid infiltration, NET formation, and tumor progression, it is not surprising that ENPP1i have emerged as potent immunostimulatory agents (44). In fact, eradicating MDSC infiltration by blocking CXCR2 also impaired NET formation and sensitized tumors to immune-checkpoint inhibitors (45). Besides HP, other factors comodulated with ENPP1 could act as chemoattractant factors for PMN-MDSC boosting the LRF phenotype. For instance, VEGFA, a component of the ENPP1-comodulated gene signature, was shown to trigger MDSC infiltration and impair T-cell function, and could favor tumor growth in more advanced stages by enhancing tumor angiogenesis. A limitation of our model was that the short time of latency did not recapitulate a more complex clinical scenario emerging >1 year after IR, in which signals emanating from healed RTB, derived from persistent TGFβ activation, could foster the recruitment of reactivated dormant or disseminated tumor cells (46).

Our new LRF model also integrates the mechanistic role of CTC in tumor recurrence. The presence of CTC frequently detected as an early event in patients with breast cancer with the increased number of CTC during surgical manipulation was also concordant in our model and supports the notion that they make a significant contribution to LRF (47). At early stages after resection, CTC were homing to the ipsi- and contralateral mammary glands to a similar extent, but only those CTC engrafting in the RTB yielded productive recurrent tumors over time. The emergence of CTC clusters within recurrent tumors suggests the requirement of cell–cell interactions as a potential mechanism involved in the competency of the "fertile soil" with fit ENPP1$^{hi}$ CTC for proficient local tumor relapse.

In line with our results, fractionated IR was advantageous mainly in patients with CTC positivity (47). Indeed, the selective obliteration of CTC prevents metastasis and extends survival (48). Beyond the cytotoxic effect of FD, the number of residual cells and intervals between fractions could affect LRF (6). However, ENPP1 emerged as a common mechanism impairing antitumor immune response in IR and non-IR conditions. Thus, our model opens new avenues to explore other previously defined roles of PMN-MDSC, including radioresistance (49, 50), angiogenesis (51), and metastatic activity (52).

Another inherent limitation of our CTC modeling approach was the impossibility to discriminate whether the unlabeled recurrent tumor cells were derived from unlabeled CTC (released from the primary tumor) or arose from the local infiltration of recalcitrant cells beyond resection margins. Our strategy could also be translated to other tumors such as sarcomas, head and neck carcinomas, and other neoplasms to reveal novel mechanistic insights where LRF represents an unmet clinical need.

In summary, our study unveils novel links with patient prognosis. The role of the ENPP1/HP axis, the relevance of CTC, tumor-secreted HP inductive role in PMN-MDSC infiltration, and NET formation by the adenosinergic pathway emerge as a novel players uncovered in LRF. The identification of new mediators paves the way for introducing novel post-radiation therapies to prevent LRF and discloses new vulnerabilities for drug development. This represents a promising avenue for therapeutic development, with wide implications in clinical practice for the treatment of breast cancer and other tumors (53).

## METHODS

### Cell Lines

ANV5 cells were originally derived from relapsed tumors after subcutaneous inoculation of mouse mammary carcinoma cells into nontransgenic FVB/N mice (a kind gift of K.L. Knutson; ref. 54). ANV5 cells were cultured in RPMI 1640 supplemented with 10 mmol/L HEPES, 1% GlutaMAX, and 1 mmol/L sodium pyruvate. The 4T1 cells were obtained from ATCC. Cells were tested monthly for *Mycoplasma* infection using MycoAlert. Cells were authenticated by PCR assessment.

***Isolation of Tumor Cells.*** Bulk tumors were minced into small fragments and digested in RPMI medium containing collagenase (1 mg/mL) and DNase (50 μg/mL) for 30 minutes at 37°C. Subsequently, fragments were mechanically disaggregated and filtered through a 70-μm cell strainer. Cells were collected by centrifugation, resuspended in complete medium, and cultured. We obtained different cell subpopulations from recurrent tumors in IR and non-IR animals.

***Isolation of CTC.*** Cells were transduced with pSIN-puro-GFP lentivirus for cell tracking. To isolate CTC-out cells, mice were orthotopically inoculated in the mammary gland with pSIN-puro-GFP–transduced 4T1 cells. Blood extraction was performed by intracardiac puncture under anesthesia in EDTA Microvette 500K3E tubes (Sarstedt). Cells were cultured in complete medium and selected with puromycin.

For CTC-in, cells were inoculated in the left cardiac ventricle in six-week female immune-compromised mice (Rag2tm1.1Flv Il2rgtm1.1Flv/J). Tumors were disaggregated to single-cell suspension, and after selection with 4 to 6 μg/mL of puromycin, CTC-in cells were cultured until single cell–derived colonies were detected. In homing experiments, cells were fixed and stained with crystal violet for 15 minutes. Colonies were counted using an automated macro developed in Fiji software (ImageJ, RRID:SCR_003070).

### Establishment of Tumor Models

All experiments were executed in compliance with institutional guidelines and regulations and after approval from the Local Animal Ethics Committee (160-14 and 114-19). Sex did not represent a biological variable in this study. All experiments were performed in female mice. Cells were resuspended in PBS:Matrigel (BD Biosciences) at 1:1 ratio. Fifty microliters containing $2 \times 10^4$ ANV5 or 4T1 cells (RRID:CVCL_0125) in Matrigel at 1:1 volume (BD Bioscience) were injected through a 1-cm-long incision into the fourth and fifth inguinal mammary fat pads of six- to seven-week-old female syngeneic FVB/N mice or BALB/c (RRID:IMSR_ORNL:BALB/cRl) mice (Envigo) for 4T1 cells. After inoculation, the skin was sutured with Vicryl 6.0. When tumors reached the indicated volume, tumors were resected and catheters were implanted until radiation (Fig. 1A). Tumors were usually detected by palpation two weeks after tumor cell inoculation. Orthotopic tumors were resected *en bloc*. Surgery aimed to completely remove all visible gross tumor. The tumor in the inguinal mammary gland was grasped between the thumb and the index finger for immobilization, and a small incision, 1–2 mm deep and 10–15 mm long, was created in the skin overlying the tumor. The tissues surrounding the index lesion (radial tumor margins) were dissected to allow mobilization. The tumor was then gently pulled out through the skin opening with a mini-forceps, and the tumor was removed from its base (deep tumor margin). The whole surface of the tumor specimen was ink-marked for pathologic assessment (Fig. 1A). A summary of the surgical margins of all experiments is included in Supplementary Table S5.

***Tumor Enrichment Phenotype.*** Cells were expanded *ex vivo* (first cycle) and reinoculated in the mammary glands of another cohort of mice, $n = 8$–10 per each cell subpopulation. After local recurrence, tumors were surgically resected, and recurrent cells were isolated and expanded *in vitro* (second cycle). Isolated first and second cycle cell subpopulations were compared to assess their "local recurrence" phenotype by evaluating the time to LRF.

### Radiation Procedure

After tumor excision, a leader Angiocath 16GA was subcutaneously implanted over the RTB to allow the insertion of a standard 6 Fr afterloading catheter CT/MR Flexible Implant Tube 6F (SL, 30 cm, Elekta), passed backward toward the former skin entry point, and then pulled outside and fixed with a stopper (plastic button). The next day, mice were anesthetized to allow the insertion of the 4 Fr catheter coupled to the afterloader (Fig. 1A). Immediately after last irradiation dose, the catheter was pulled out for the rest of the experimental period. Brachytherapy treatment was used with predefined

CT-based standards to deliver an SD of 15 Gy to the CTVD$_{90}$ (minimum dose received by 90% or the CTV). Standards were generated previously using several implanted mice for CT image acquisition at 1 mm intervals. For non-IR conditions, surgery and the catheter placement were performed as in IR animals. The standard CTV created was 20 mm long in the axis of the catheter with a diameter of 10 mm. In fractionated irradiation, four fractions of 6.2 Gy each, twice a day, at least six hours apart were delivered over two consecutive days to reach a total dose of 24.8 Gy. SD irradiation of 15 Gy and fractionated irradiation of 24.8 Gy (6.2 Gy × 4) are equi-effective as per the linear-quadratic formulation.

### Overexpressed and Silenced Cells

Gene silencing was performed by lentiviral infection using shRNA in pLKO.1 vector (RRID:Addgene_52920) as previously described (55). For gene overexpression, mouse cDNA encoding ENPP1 was cloned into pBABE-Neo as described (RRID:Addgene_1767; ref. 56).

### Purification of PMN-MDSC

We performed experiments using PMN-MDSC obtained by two different procedures:

1. Purification of spleen-derived PMN-MDSC was performed by immunomagnetic positive selection from mice carrying 21-day Lewis lung cell carcinoma tumors with Ly6G microbead kit (Miltenyi RRID: AB_2895065) according to the manufacturer's recommendations.
2. Differentiated PMN-MDSC obtained from murine bone marrow were generated as previously described (57). Briefly, mononuclear precursors were obtained from bone marrow of 8- to 12-week-old female C57BL/6J mice (RRID:IMSR_JAX:000664) and cultured in complete medium for 24 hours. Nonadherent cells were recovered 24 hours after extraction and reseeded. These cells were incubated for 7 days with 50% CM obtained from 3-day culture of $8 \times 10^5$ genetically modified Lewis lung carcinoma cells and 50% complete medium. Adherent cells were harvested with PBS with 1 mmol/L EDTA and were used for flow cytometry analyses.

### Invasion Assays

The upper wells of 8-μm-pore-size Boyden chambers were coated with MDSC stained with Hoechst (1:1,000 dilution, Thermo Fisher Scientific) at a density of $10^3$ cells/μL embedded in hydrogel composed by type 1 collagen (2 mg/mL, BD Bioscience) and Matrigel poor in growth factors (2 mg/mL, BD Bioscience) as previously described (58). HP was used at a concentration of 0.02 to 0.5 mg/mL based on the findings that murine serum levels are between 0.5 and 1.5 mg/mL in normal conditions. After 24 hours, cells were recovered from the lower chamber and were quantified by flow cytometry using a CytoFLEX (Beckman Coulter) and CyteExpert software. Experiments were repeated three times.

### NET Formation Assay

*In vitro*–differentiated murine MDSC ($1 \times 10^6$ cells) stained with Hoechst (20 μmol/L, Thermo Fisher) and calcein (1 mg/mL diluted 1:2,000, Invitrogen) were cocultured with the indicated tumor cells (ANV5, 4T1, or derivatives), previously stained with orange CMRA (1 mg/mL, diluted 1:2,000, Invitrogen) and Hoechst. The coculture was embedded at $10^3$ cells/μL in hydrogels. After 48 hours (for mouse cells) and 20 hours (for human cells), images were captured by a confocal microscope LSM 800 laser-scanning (Carl Zeiss) with Plan-apochromat-63×. Images in Z were acquired with Zen 2.3 software (Carl Zeiss) and were visualized with Volocity 3D (RRID:SCR_002668, Thermo Fisher Scientific). NET area and the percentage of NETs were calculated using the plugin DANA for ImageJ (developed by Dr. Miriam Shelef, University of Wisconsin–Madison, Madison, WI). At least 60 cells per experimental condition were analyzed (59). Experiments were repeated three times.

### Assessment of ENPP1 Activity

A day before the assay, cells were seeded at $5 \times 10^4$ cells per well in 96-well plates. The next day, culture media were replaced by 50 μL of the buffer assay (50 mmol/L Tris, 250 mmol/L NaCl, pH 9.5). Subsequently, 50 μL of the assay buffer containing the reagent thymidine 5′-monophosphate p-nitrophenyl ester (Sigma, #T4510) at 10 mmol/L diluted in deionized water was added in each well. Absorbance was measured at 405 nm over time. Measurements were taken after 60-minute reaction.

### Analysis of NET in Tissue Sections

Evaluation of NETs was performed using an Automated Quantitative Pathology Imaging System (Vectra Polaris, Akoya Biosciences). Tissue imaging and spectral unmixing were performed using inForm software (version 2.4.8, Akoya Biosciences). Image analysis was then performed using the open-source digital pathology software QuPath version 0.2.3 and ImageJ Software, an open-source Java-based image processing software. Measurement workflow and scoring have been previously described (42). In short, neutrophils were identified by the costaining with CD15 and MPO. NETs were detected based on the costaining with CD15, MPO, and H3Cit. An ImageJ software plugin was developed and validated to accurately calculate the percentage area of neutrophils and NETs for each TMA spot (42).

### BLI Evaluation

We used *Rag2*$^{-/-}$/*Il2Rγ*$^{-/-}$ in-house bred mice (Rag2tm1.1Flv Il2rgtm1.1Flv/J, Jackson Labs, RRID:IMSR_JAX:014593) to avoid immune recognition in preliminary experiments to improve the surgical procedure. Cells were transduced with triple modality (GFP-luciferase-Δ45HSV1-tk; refs. 55, 56) or pSIN-puro-GFP lentiviruses. BLI evaluation was performed immediately after surgery under anesthesia after inoculation of 50 μL of 15 mg/mL D-Luciferin into the retro-orbital plexus for assessment of residual disease as well as during follow-up for detection of local relapse or distant spread. The date of local relapse was registered as the date of the first positive BLI test post-surgery or the date of the first palpable recurrence post-surgery in those cases with weak or negative bioluminescence. Images were captured immediately after injection during one minute with PhotonIMAGER imaging system (Biospace Lab) and analyzed using M3Vision software (Biospace Lab). Photon flux was calculated for each mouse using a region of interest for each mammary gland inoculated. All BLI signals were normalized with values from day 0.

### Histologic Evaluation

Mammary tumors were formalin-fixed for 24 hours and maintained in 70% ethanol, dehydrated, and paraffin-embedded according to standard protocols conducted at the Morphology Core Facility at CIMA. Five-micrometer sections were stained in hematoxylin and eosin (H&E). Ink-marked margins were evaluated for each tumor by an experienced pathologist. Resections were categorized into R0 (clear margins in all directions), R1 (focally involved surgical margin), and R2 (extensively involved surgical margins). For IHC, the anti-GFP antibody (ab6556) was used in serial sections. For TMA, anti-ENPP1 antibody was used at 1:4,000 dilution (ab40003). The detection of Gr1$^+$ cells was performed with an anti-Gr1 antibody (BioLegend, ref. 108402) at 1:5,000 dilution. IHC staining was performed using EnVision (Dako) and revealed using diaminobenzidine (DAB). Whole mount sections were acquired and digitized using Leica Aperio CS2 system. Image analysis was performed with Fiji software (RRID:SCR_002285).

### Multiplexed Immunofluorescence Staining

The optimization and validation workflow of the multiplex immunolabeling protocol development has been previously described (42). A five-color multiplex quantitative immunofluorescence assay for formalin-fixed, paraffin-embedded tissue human specimens was implemented for simultaneous detection of the granulocyte marker CD15, the neutrophil marker MPO, H3Cit, cytokeratin (CK), and DAPI. Briefly, TMA sections were deparaffinized and subjected to sequential rounds of antibody staining. Antigen retrieval was performed using DAKO PT-Link heat-induced antigen retrieval with low pH (pH = 6) or high pH (pH = 9) target retrieval solution (DAKO). Antibodies were CD15 (mouse monoclonal, clone Carb-3, 1:100, Agilent, product # IR062, RRID:AB_10838679), MPO (rabbit monoclonal, clone E1E7I, isotype IgG, 1:2,000, Cell Signaling, product # 14569S, RRID:AB_2798516), anti-histone H3 citrullinated (citrulline R2 + R8 + R17, H3Cit) antibody (rabbit polyclonal, 1:100, Abcam, product # ab5103, RRID:AB_304752), and CK wide spectrum screening (1:100, Agilent, product # Z0622). Tyramide signal amplification with fluorophores Opal 620 and Opal 690 was used for visualization of CD15 and H3Cit, respectively. Cy3 Tyramide Plus (1:100) and Alexa488 were used for visualization of MPO and CK, respectively. Thereafter, nuclei were counterstained with spectral DAPI (Akoya Bioscience). Sections were then mounted with Faramount Aqueous Mounting Medium (Dako).

### Western Blot Analysis

Cells were lysed in RIPA-buffer [1% Nonident P-40, 50 mmol/L Tris-HCl (pH 7.4), and 150 mmol/L NaCl] supplemented with protease inhibitors (Sigma). Protein lysates were subjected to 6% SDS-PAGE, transferred to nitrocellulose membrane (Bio-Rad), and incubated with anti-ENPP1 (PA5-17097, Invitrogen), anti-EPAS1 (sc-13596, Santa Cruz, RRID:AB_627525), anti-SRPX2 (Ab01584, Abcam), anti-APCDD1 (sc-84694, Santa Cruz, RRID:AB_2057638), anti-HP (ab256454, Abcam), and anti-tubulin antibody (T4026, Sigma-Aldrich). Bands were developed with enhanced chemiluminescence system (Amersham Bioscience).

### Blood Extraction and Evaluation

Blood extracted by cardiac puncture under anesthesia was recovered into sterile cell-free DNA BCT, EDTA-glass tubes (Streck) and analyzed by Parsortix Technology (Angle). Blood parameters were assessed by Hemavet 950 counter (Drew Scientific Inc).

### Flow Cytometry Analysis

Tumors were dissected, cut into small pieces, and incubated with collagenase/DNase buffer (as previously described) for 30 minutes and mechanically disaggregated through 70-µm cell strainer. Erythrocytes were lysed (red blood cell lysis buffer, Sigma), and cell suspensions were harvested with Percoll 35% (GE Healthcare). One million cells were treated with CD16/CD32 (Mouse BD Fc Block, 1:200, clone 2.4G2, BD Bioscience) and stained on ice with the following fluorochrome-conjugated antibodies: anti-mouse CD45 (APC-H7, 1:500, clone 30-F11, BioLegend), CD11b (BUV661, 1:160 clone M1/70, BD Bioscience), CD11c (BUV395, 1:80, clone HL3, BD Bioscience), Ly6G (AF700, 1:200, clone 1A8, BioLegend), Ly6C (BV510, 1:200, clone HK1.4, BioLegend), F4/80 (BV605, 1:80, clone BM8, BioLegend), MHC-C2 (BV650, 1:80, clone M5/114.15.2, BioLegend), CD38 (PerCP/Cy5,5, 1:160, clone 90, BioLegend), and CD8 (BUV395, 1:200, clone 53–6.7, BD Bioscience), CD44 (BV510, 1:200, clone IM7, BioLegend), CD62 L (AF700, 1:800, clone MEL-14, BioLegend), CD4 (BUV496, 1:400, clone GK1.5, BD Bioscience), CD25 (PerCP/Cy5,5, 1:50, clone PC61, BioLegend), CD19 (BUV661, 1:200 clone 1D3, BD Bioscience), NKp46 (CD335; APC, 1:20, clone 29A1.4, BioLegend), LAG3 (BV650, 1:400, clone C9B7W, BioLegend), GITR (FITC, 1:100, clone DTA-1, BioLegend), and PD-1 (BV605, 1:80, clone 29F.1A12, BioLegend) diluted in FACS buffer (PBS, 0.24 mmol/L EDTA, and 5% serum FetalClone). For intracellular staining, cells were permeabilized after surface staining with eBioscience Fixation/Permeabilization Kit for 15 minutes and intracellularly stained with GzB (BV421, 1:20, clone GB11, BioLegend), FOXP3 (PECy7, 1:320, clone 3G3, Abcam) and CD206 (PECy7, 1:40, clone C068C2, BioLegend). Dead cells were excluded using PromoFluor-840 NIR Maleimide (PromoCell). Cells were acquired using a CytoFLEX LX flow cytometer (Beckman Coulter) and analyzed with CytExpert software (RRID:SCR_017217). Gating strategy of flow cytometry analysis is shown in Supplementary Fig. S5.

### Microarray Data Analysis: Normalization and Gene-Expression Calculation

Normalization of microarray data (Affymetrix Mouse Gene 2.0 ST) was performed with robust multiarray average algorithm (RMA; ref. 60). After quality assessment and outlier detection with R/Bioconductor, a filtering process was carried out to eliminate low expression probe sets (61). Applying the criterion of an expression value greater than 16 in at least 50% of the samples of one of the experimental conditions, 18,311 probe sets were selected for statistical analysis. Linear models for microarray data (LIMMA; ref. 62) were used to identify the probe sets that showed significant differential expression between experimental conditions. Hierarchical clustering of microarray data was performed using R (63).

### RNA-seq Data Analysis

Quality of the samples was verified using FastQC (RRID:SCR_014583) software https://www.bioinformatics.babraham.ac.uk/projects/fastqc/. The alignment of reads to the mouse genome (mm10) was performed using STAR (ref. 64; RRID:SCR_004463). Subsequently, gene-expression quantification using read counts of exonic gene regions was carried out with feature Counts (65), and the gene annotation reference was Gencode M25 (66). Differential expression statistical analysis was performed using R/Bioconductor.

First, gene-expression data were normalized with edgeR (ref. 67; RRID:SCR_012802) and voom (62). After quality assessment and outlier detection using R/Bioconductor (RRID:SCR_006442), a filtering process was performed. Genes with read counts lower than 6 in more than the 50% of the samples of all the studied conditions were considered as not expressed in the experiment under study. LIMMA (RRID:SCR_010943) were used to identify the genes with significant differential expression between experimental conditions. Genes were selected as differentially expressed using a $B > 0$ cutoff. Further functional and clustering analyses and graphical representations were performed using R/Bioconductor. The selection of coherent changes caused by ENPP1 silencing or overexpression was based in a $P$ value cutoff $P < 0.05$ in all the experiments and coherent logFC changes between experiments. The clustering analysis of these genes was performed with transformed expression data on the same scale making comparable different experiments.

### Patients and Tissue Samples

*In silico* analysis was performed with patients with breast cancer included in the Kaplan–Meier plotter (http://kmplot.com/analysis/), a web-based tool that uses transcriptomic data.

Selection was performed from the archives of the Clínica Universidad de Navarra (CUN) from 1995 to 2017. Inclusion criteria included all available archival material examined for integrity and representative areas of H&E-stained tumors selected by an expert pathologist. We included only TNBC and HER2$^+$ subtypes from patients who were surgically resected and irradiated. We excluded patients for whom material was unavailable or deteriorated. The protocol was approved by the Research Ethics Committee of the University of Navarra (reference 2019.180 y el 2019.181), and written informed consent was obtained from all living patients or the closest relative in the case of deceased patients. Clinical features of patients are specified in Supplementary Table S4. IHC analysis was performed in this cohort of primary naïve breast cancer tumors and local recurrences obtained from patients with breast cancer at the CUN. Tumors were fixed in 10% buffered formalin after surgical removal and paraffin-embedded using standard protocols. Tumors were classified according to the World Health Organization 2004 classification. For survival analysis, RFS and overall survival were calculated from the date of surgery to the date of recurrence or death according to the clinical information. For the evaluation, an H-score was calculated after IHC analysis by two expert pathologists in blind records. Patients were stratified into two groups according to the median of ENPP1 H-score.

***Development of Breast Cancer TMAs.*** The TMAs included 114 samples derived from 56 paired samples (primary and LRF) obtained from 28 patients (HER2$^+$, $n = 18$; TNBC, $n = 10$) who failed locoregionally, and 48 single samples of HER2$^+$ ($n = 24$) or TNBC ($n = 24$) patients who remained disease free for at least three years of follow-up after primary treatment. It also included 10 unpaired samples of TNBC or HER2$^+$ patients who relapsed locally or elsewhere (TNBC, $n = 8$; HER2$^+$, $n = 2$). In total, four TMAs were constructed using a 1-mm diameter needle in a manual tissue arrayer (MTA-1, Beecher Instruments). For better representation of the tumors, three cores obtained from different areas were included in the TMA. Consecutive 3-μm sections were obtained. TMAs were constructed by the Morphology Core Facility at the CIMA (Pamplona, Spain).

### Statistical Analysis

Statistical analysis was performed using GraphPad Prism 8.0. Survival curves were compared with log-rank test. Differences among groups were analyzed either by one-way ANOVA followed by Tukey *post hoc* test or by Brown–Forsythe and Tamhane T2 test. For nonparametric statistics, data were analyzed by Kruskal–Wallis test followed by Mann–Whitney multiple comparisons test with Bonferroni adjustment. Student *t* test was used where indicated.

Reagent tables are included in the Supplementary Section.

### Data Availability

All RNA-seq and microarray data have been deposited in the Gene Expression Omnibus (accession number GSE193692).

## Authors' Disclosures

N. Perurena reports other support from the Government of Spain during the conduct of the study. T. Walle reports grants from the European Commission, German Cancer Aid, and the German Cancer Research Center during the conduct of the study; grants from CanVirex outside the submitted work; and stock ownership in Roche, BionTech, Bayer AG, and AstraZeneca. V. Strnad reports grants, personal fees, and nonfinancial support from Nucletron Operations B.V., an Elekta Company, and personal fees from Siemens outside the submitted work. I. Melero reports grants and personal fees from Bristol Myers Squibb, Roche, Alligator, AstraZeneca, and Genmab, and personal fees from F-Star, Numab, Gossamer, Hotspot, Highlight Therapeutics, Biolinerx, and Amunix outside the submitted work. No disclosures were reported by the other authors.

## Authors' Contributions

**B. Ruiz-Fernández de Córdoba:** Formal analysis, validation, investigation, visualization, methodology, writing–original draft, writing–review and editing. **H. Moreno:** Data curation, formal analysis, funding acquisition, validation, investigation, visualization, methodology. **K. Valencia:** Data curation, validation, investigation, methodology, writing–review and editing. **N. Perurena:** Investigation, writing–review and editing. **P. Ruedas:** Formal analysis, validation, investigation. **T. Walle:** Data curation, formal analysis, validation, investigation. **A. Pezonaga-Torres:** Validation, investigation, visualization, methodology. **J. Hinojosa:** Validation, investigation, methodology. **E. Guruceaga:** Data curation, software, formal analysis. **A. Pineda-Lucena:** Investigation, methodology. **M. Abengózar-Muela:** Resources, data curation, investigation, visualization. **D. Cochonneau:** Investigation, visualization, methodology. **C. Zandueta:** Investigation, visualization, methodology. **S. Martínez-Canarias:** Validation, investigation, visualization. **A. Teijeira:** Validation, investigation, visualization, methodology, writing–review and editing. **D. Ajona:** Investigation, methodology, writing–original draft, project administration. **S. Ortiz-Espinosa:** Validation, investigation, visualization, methodology. **X. Morales:** Data curation, validation, investigation, visualization, methodology. **C. Ortiz de Solórzano:** Validation, writing–review and editing. **M. Santisteban:** Resources, writing–original draft. **L.I. Ramos-García:** Data curation, software, formal analysis. **L. Guembe:** Validation, investigation, methodology. **V. Strnad:** Investigation, visualization, methodology. **D. Heymann:** Formal analysis, validation, investigation, visualization, methodology. **S. Hervás-Stubbs:** Formal analysis, validation, investigation, visualization, methodology. **R. Pío:** Validation, methodology. **M.E. Rodríguez-Ruiz:** Data curation, formal analysis, investigation, methodology. **C.E. de Andrea:** Resources, data curation, supervision, validation, investigation, visualization, methodology. **S. Vicent:** Resources, validation, investigation, visualization, methodology, writing–review and editing. **I. Melero:** Formal analysis, investigation, methodology, writing–review and editing. **F. Lecanda:** Conceptualization, resources, formal analysis, supervision, funding acquisition, writing–original draft, project administration, writing–review and editing. **R. Martínez-Monge:** Conceptualization, resources, formal analysis, supervision, funding acquisition, investigation, writing–original draft, project administration, writing–review and editing.

## Acknowledgments

This work was supported by FIMA, the Fondo de Investigación Sanitaria-Fondo Europeo de Desarrollo Regional “Una manera de hacer Europa” to R. Martínez-Monge (PI16/01847, PI19/01884, PI17/00411, and PI20/00419), Foundation AECC (PRYES211377MART), and the Gobierno de Navarra (ref. 34/2021). F. Lecanda was funded by Cancer Research Thematic Network of the Instituto de Salud Carlos III (RTICC RD12/0036/0066), SAF2015-71606R, RTI2018-094507-B-100 financed by MCIN/AEI/10.13039/501100011033 and by FEDER “Una manera de hacer Europa.” F. Lecanda was also funded by “la Caixa” Foundation, Caja Navarra Foundation, and the Foundation AECC (PROYE20083LECA). This study was also supported by the Foundation for Applied Medical Research (FIMA) and CIBERONC (CB16/12/00443). S. Vicent was supported by the Spanish Ministry of Economy and Competitiveness (MINECO, SAF2013-46423-R and SAF2017-89944-R), the European Commission (618312 KRASmiR FP7-PEOPLE-2013-CIG), Worldwide Cancer Research (16-0224), Red Temática de Investigación Cooperativa en Cáncer (RD12/0036/0040), La Caixa-FIMA agreement, ANOC, and Maria Eugenia Burgos de la Iglesia's family. C.O. de Solórzano was supported by the Spanish Ministry of Science, Innovation and Universities (RTI2018-094494-B-C22 and RTC-2017-6218-1; MCIU/AEI/FEDER, UE). The authors wish to thank Mrs. Ruth Breeze for editorial assistance. We are indebted to the members of the Morphology and Image Core facility, especially Cristina Ederra and Mikel Ariz and all members of the Animal Core Facility at CIMA. Graphics were designed with the free version of BioRender.

The costs of publication of this article were defrayed in part by the payment of page charges. This article must therefore be hereby marked *advertisement* in accordance with 18 U.S.C. Section 1734 solely to indicate this fact.

Received July 16, 2021; revised November 15, 2021; accepted January 18, 2022; published first January 27, 2022.

## REFERENCES

1. Siegel RL, Miller KD, Jemal A. Cancer statistics, 2017. CA Cancer J Clin 2017;67:7–30.
2. Liu FF, Shi W, Done SJ, Miller N, Pintilie M, Voduc D, et al. Identification of a low-risk luminal a breast cancer cohort that may not benefit from breast radiotherapy. J Clin Oncol 2015;33:2035–40.
3. Kyndi M, Sorensen FB, Knudsen H, Overgaard M, Nielsen HM, Overgaard J, et al. Estrogen receptor, progesterone receptor, HER-2, and response to postmastectomy radiotherapy in high-risk breast cancer: the Danish Breast Cancer Cooperative Group. J Clin Oncol 2008;26:1419–26.
4. Early Breast Cancer Trialists' Collaborative G, Darby S, McGale P, Correa C, Taylor C, Arriagada R, et al. Effect of radiotherapy after breast-conserving surgery on 10-year recurrence and 15-year breast cancer death: meta-analysis of individual patient data for 10,801 women in 17 randomised trials. Lancet 2011;378:1707–16.
5. Krause M, Dubrovska A, Linge A, Baumann M. Cancer stem cells: radioresistance, prediction of radiotherapy outcome and specific targets for combined treatments. Adv Drug Deliv Rev 2017;109:63–73.
6. Belletti B, Vaidya JS, D'Andrea S, Entschladen F, Roncadin M, Lovat F, et al. Targeted intraoperative radiotherapy impairs the stimulation of breast cancer cell proliferation and invasion caused by surgical wounding. Clin Cancer Res 2008;14:1325–32.
7. Husemann Y, Geigl JB, Schubert F, Musiani P, Meyer M, Burghart E, et al. Systemic spread is an early step in breast cancer. Cancer Cell 2008;13:58–68.
8. Janni WJ, Rack B, Terstappen LW, Pierga JY, Taran FA, Fehm T, et al. Pooled analysis of the prognostic relevance of circulating tumor cells in primary breast cancer. Clin Cancer Res 2016;22:2583–93.
9. Rack B, Schindlbeck C, Juckstock J, Andergassen U, Hepp P, Zwingers T, et al. Circulating tumor cells predict survival in early average-to-high risk breast cancer patients. J Natl Cancer Inst 2014;106:dju066.
10. Pantel K, Alix-Panabieres C. Circulating tumour cells in cancer patients: challenges and perspectives. Trends Mol Med 2010;16:398–406.
11. Trapp E, Janni W, Schindlbeck C, Juckstock J, Andergassen U, de Gregorio A, et al. Presence of circulating tumor cells in high-risk early breast cancer during follow-up and prognosis. J Natl Cancer Inst 2018;111:380–7.
12. Rossi E, Basso U, Celadin R, Zilio F, Pucciarelli S, Aieta M, et al. M30 neoepitope expression in epithelial cancer: quantification of apoptosis in circulating tumor cells by CellSearch analysis. Clin Cancer Res 2010;16:5233–43.
13. Kim MY, Oskarsson T, Acharyya S, Nguyen DX, Zhang XH, Norton L, et al. Tumor self-seeding by circulating cancer cells. Cell 2009;139:1315–26.
14. Gabrilovich DI, Nagaraj S. Myeloid-derived suppressor cells as regulators of the immune system. Nat Rev Immunol 2009;9:162–74.
15. Condamine T, Ramachandran I, Youn JI, Gabrilovich DI. Regulation of tumor metastasis by myeloid-derived suppressor cells. Annu Rev Med 2015;66:97–110.
16. Onyedibe KI, Wang M, Sintim HO. ENPP1, an old enzyme with new functions, and small molecule inhibitors: a STING in the tale of ENPP1. Molecules 2019;24:4192.
17. Li L, Yin Q, Kuss P, Maliga Z, Millan JL, Wu H, et al. Hydrolysis of 2′3′-cGAMP by ENPP1 and design of nonhydrolyzable analogs. Nat Chem Biol 2014;10:1043–8.
18. Kato K, Nishimasu H, Oikawa D, Hirano S, Hirano H, Kasuya G, et al. Structural insights into cGAMP degradation by Ecto-nucleotide pyrophosphatase phosphodiesterase 1. Nat Commun 2018;9:4424.
19. Carozza JA, Böhnert V, Nguyen KC, Skariah G, Shaw KE, Brown JA, et al. Extracellular cGAMP is a cancer-cell-produced immunotransmitter involved in radiation-induced anticancer immunity. Nat Cancer 2020;1:184–96.
20. Sharif T, Ahn DG, Liu RZ, Pringle E, Martell E, Dai C, et al. The NAD(+) salvage pathway modulates cancer cell viability via p73. Cell Death Differ 2016;23:669–80.
21. Vaisitti T, Audrito V, Serra S, Bologna C, Brusa D, Malavasi F, et al. NAD+-metabolizing ecto-enzymes shape tumor-host interactions: the chronic lymphocytic leukemia model. FEBS Lett 2011;585:1514–20.
22. Horenstein AL, Chillemi A, Quarona V, Zito A, Roato I, Morandi F, et al. NAD(+)-metabolizing ectoenzymes in remodeling tumor-host interactions: the human myeloma model. Cells 2015;4:520–37.
23. Rittiner JE, Korboukh I, Hull-Ryde EA, Jin J, Janzen WP, Frye SV, et al. AMP is an adenosine A1 receptor agonist. J Biol Chem 2012; 287:5301–9.
24. Young A, Mittal D, Stagg J, Smyth MJ. Targeting cancer-derived adenosine: new therapeutic approaches. Cancer Discov 2014;4:879–88.
25. Papayannopoulos V. Neutrophil extracellular traps in immunity and disease. Nat Rev Immunol 2018;18:134–47.
26. Talbot J, Bianchini FJ, Nascimento DC, Oliveira RD, Souto FO, Pinto LG, et al. CCR2 expression in neutrophils plays a critical role in their migration into the joints in rheumatoid arthritis. Arthritis Rheumatol 2015;67:1751–9.
27. Shinde-Jadhav S, Mansure JJ, Rayes RF, Marcq G, Ayoub M, Skowronski R, et al. Role of neutrophil extracellular traps in radiation resistance of invasive bladder cancer. Nat Commun 2021;12:2776.
28. Wisdom AJ, Hong CS, Lin AJ, Xiang Y, Cooper DE, Zhang J, et al. Neutrophils promote tumor resistance to radiation therapy. Proc Natl Acad Sci U S A 2019;116:18584–9.
29. Vanpouille-Box C, Alard A, Aryankalayil MJ, Sarfraz Y, Diamond JM, Schneider RJ, et al. DNA exonuclease Trex1 regulates radiotherapy-induced tumour immunogenicity. Nat Commun 2017;8:15618.
30. Li J, Duran MA, Dhanota N, Chatila WK, Bettigole SE, Kwon J, et al. Metastasis and immune evasion from extracellular cGAMP hydrolysis. Cancer Discov 2020;11:1212–27.
31. Levy AP, Asleh R, Blum S, Levy NS, Miller-Lotan R, Kalet-Litman S, et al. Haptoglobin: basic and clinical aspects. Antioxid Redox Signal 2010;12:293–304.
32. Wirsdorfer F, de Leve S, Cappuccini F, Eldh T, Meyer AV, Gau E, et al. Extracellular adenosine production by ecto-5′-nucleotidase (CD73) enhances radiation-induced lung fibrosis. Cancer Res 2016;76:3045–56.
33. Wennerberg E, Spada S, Rudqvist NP, Lhuillier C, Gruber S, Chen Q, et al. CD73 blockade promotes dendritic cell infiltration of irradiated tumors and tumor rejection. Cancer Immunol Res 2020;8:465–78.
34. Marcus A, Mao AJ, Lensink-Vasan M, Wang L, Vance RE, Raulet DH. Tumor-derived cGAMP triggers a STING-mediated interferon response in non-tumor cells to activate the NK cell response. Immunity 2018;49:754–63.
35. Abbasi S, Shin DM, Beaty N, Masiuk M, Chen S, Gonzalez-Garcia I, et al. Characterization of monoclonal antibodies to the plasma cell alloantigen ENPP1. Hybridoma 2011;30:11–7.
36. Sinha P, Clements VK, Bunt SK, Albelda SM, Ostrand-Rosenberg S. Cross-talk between myeloid-derived suppressor cells and macrophages subverts tumor immunity toward a type 2 response. J Immunol 2007;179:977–83.
37. Teijeira A, Garasa S, Ochoa MDC, Cirella A, Olivera I, Glez-Vaz J, et al. Differential interleukin-8 thresholds for chemotaxis and netosis in human neutrophils. Eur J Immunol 2021;51:2274–80.
38. Oh SK, Pavlotsky N, Tauber AI. Specific binding of haptoglobin to human neutrophils and its functional consequences. J Leukoc Biol 1990;47:142–8.
39. Cools-Lartigue J, Spicer J, McDonald B, Gowing S, Chow S, Giannias B, et al. Neutrophil extracellular traps sequester circulating tumor cells and promote metastasis. J Clin Invest 2013;123: 3446–58.
40. Teijeira A, Garasa S, Gato M, Alfaro C, Migueliz I, Cirella A, et al. CXCR1 and CXCR2 chemokine receptor agonists produced by

tumors induce neutrophil extracellular traps that interfere with immune cytotoxicity. Immunity 2020;52:856–71.

41. Park J, Wysocki RW, Amoozgar Z, Maiorino L, Fein MR, Jorns J, et al. Cancer cells induce metastasis-supporting neutrophil extracellular DNA traps. Sci Transl Med 2016;8:361ra138.
42. de Andrea CE, Ochoa MC, Villalba-Esparza M, Teijeira A, Schalper KA, Abengozar-Muela M, et al. Heterogenous presence of neutrophil extracellular traps in human solid tumours is partially dependent on interleukin-8. J Pathol 2021;255:190–201.
43. Alfaro C, Teijeira A, Onate C, Perez G, Sanmamed MF, Andueza MP, et al. Tumor-produced interleukin-8 attracts human myeloid-derived suppressor cells and elicits extrusion of neutrophil extracellular traps (NETs). Clin Cancer Res 2016;22:3924–36.
44. Carozza JA, Brown JA, Bohnert V, Fernandez D, AlSaif Y, Mardjuki RE, et al. Structure-aided development of small-molecule inhibitors of ENPP1, the extracellular phosphodiesterase of the immunotransmitter cGAMP. Cell Chem Biol 2020;27:1347–58.
45. Highfill SL, Cui Y, Giles AJ, Smith JP, Zhang H, Morse E, et al. Disruption of CXCR2-mediated MDSC tumor trafficking enhances anti–PD-1 efficacy. Sci Transl Med 2014;6:237ra67.
46. Ma L, Gonzalez-Junca A, Zheng Y, Ouyang H, Illa-Bochaca I, Horst KC, et al. Inflammation mediates the development of aggressive breast cancer following radiotherapy. Clin Cancer Res 2021;27:1778–91.
47. Goodman CR, Seagle BL, Friedl TWP, Rack B, Lato K, Fink V, et al. Association of circulating tumor cell status with benefit of radiotherapy and survival in early-stage breast cancer. JAMA Oncol 2018;4:e180163.
48. Kim YR, Yoo JK, Jeong CW, Choi JW. Selective killing of circulating tumor cells prevents metastasis and extends survival. J Hematol Oncol 2018;11:114.
49. Shen H, Song Y, Colangelo CM, Wu T, Bruce C, Scabia G, et al. Haptoglobin activates innate immunity to enhance acute transplant rejection in mice. J Clin Invest 2012;122:383–7.
50. Huntoon KM, Wang Y, Eppolito CA, Barbour KW, Berger FG, Shrikant PA, et al. The acute phase protein haptoglobin regulates host immunity. J Leukoc Biol 2008;84:170–81.
51. Coffelt SB, Wellenstein MD, de Visser KE. Neutrophils in cancer: neutral no more. Nat Rev Cancer 2016;16:431–46.
52. Wculek SK, Malanchi I. Neutrophils support lung colonization of metastasis-initiating breast cancer cells. Nature 2015;528:413–7.
53. Janot F, de Raucourt D, Benhamou E, Ferron C, Dolivet G, Bensadoun RJ, et al. Randomized trial of postoperative reirradiation combined with chemotherapy after salvage surgery compared with salvage surgery alone in head and neck carcinoma. J Clin Oncol 2008;26:5518–23.
54. Knutson KL, Lu H, Stone B, Reiman JM, Behrens MD, Prosperi CM, et al. Immunoediting of cancers may lead to epithelial to mesenchymal transition. J Immunol 2006;177:1526–33.
55. Luis-Ravelo D, Anton I, Zandueta C, Valencia K, Pajares MJ, Agorreta J, et al. RHOB influences lung adenocarcinoma metastasis and resistance in a host-sensitive manner. Mol Oncol 2014;8:196–206.
56. Luis-Ravelo D, Anton I, Zandueta C, Valencia K, Ormazabal C, Martinez-Canarias S, et al. A gene signature of bone metastatic colonization sensitizes for tumor-induced osteolysis and predicts survival in lung cancer. Oncogene 2014;33:5090–9.
57. Liechtenstein T, Perez-Janices N, Gato M, Caliendo F, Kochan G, Blanco-Luquin I, et al. A highly efficient tumor-infiltrating MDSC differentiation system for discovery of anti-neoplastic targets, which circumvents the need for tumor establishment in mice. Oncotarget 2014;5:7843–57.
58. Anguiano M, Castilla C, Maska M, Ederra C, Pelaez R, Morales X, et al. Characterization of three-dimensional cancer cell migration in mixed collagen-Matrigel scaffolds using microfluidics and image analysis. PLoS One 2017;12:e0171417.
59. Rebernick R, Fahmy L, Glover C, Bawadekar M, Shim D, Holmes CL, et al. DNA area and NETosis analysis (DANA): a high-throughput method to quantify neutrophil extracellular traps in fluorescent microscope images. Biol Proced Online 2018;20:7.
60. Irizarry RA, Bolstad BM, Collin F, Cope LM, Hobbs B, Speed TP. Summaries of Affymetrix GeneChip probe level data. Nucleic Acids Res 2003;31:e15.
61. Gentleman RC, Carey VJ, Bates DM, Bolstad B, Dettling M, Dudoit S, et al. Bioconductor: open software development for computational biology and bioinformatics. Genome Biol 2004;5:R80.
62. Ritchie ME, Phipson B, Wu D, Hu Y, Law CW, Shi W, et al. limma powers differential expression analyses for RNA-sequencing and microarray studies. Nucleic Acids Res 2015;43:e47.
63. Gene Ontology C, Blake JA, Dolan M, Drabkin H, Hill DP, Li N, et al. Gene Ontology annotations and resources. Nucleic Acids Res 2013;41(Database issue):D530–5.
64. Dobin A, Davis CA, Schlesinger F, Drenkow J, Zaleski C, Jha S, et al. STAR: ultrafast universal RNA-seq aligner. Bioinformatics 2013;29:15–21.
65. Liao Y, Smyth GK, Shi W. featureCounts: an efficient general purpose program for assigning sequence reads to genomic features. Bioinformatics 2014;30:923–30.
66. Harrow J, Frankish A, Gonzalez JM, Tapanari E, Diekhans M, Kokocinski F, et al. GENCODE: the reference human genome annotation for the ENCODE project. Genome Res 2012;22:1760–74.
67. Robinson MD, McCarthy DJ, Smyth GK. edgeR: a bioconductor package for differential expression analysis of digital gene expression data. Bioinformatics 2010;26:139–40.